

The influence of alloying elements on the chlorine-induced high temperature corrosion of Fe-Cr alloys in oxidizing atmospheres

Der Einfluß von Legierungselementen auf die chlorinduzierte Hochtemperaturkorrosion von Fe-Cr-Legierungen in oxidierender Atmosphäre

A. Zahs, M. Spiegel and H. J. Grabke*

The effect of the alloying elements Al, Cr, Mn, Mo, Si and Ti on the corrosion behaviour of ferritic Fe-15Cr model alloys was studied in a N_2/He -5 vol.% O_2 gas mixture with and without additions of 500–1500 vppm HCl at 600 °C. The main corrosion mechanism is "active oxidation", characterized by the formation of volatile metal chlorides at the metal/oxide interface. Volatilization and subsequent conversion of the chlorides into oxides results in the formation of porous and poorly adherent oxide scales. Large mass gains were observed for Fe-15Cr, Fe-35Cr and Fe-15Cr with additions of 5 wt.% Ti, 10 wt.% Mn or 10 wt.% Mo. The specific morphology of the corrosion products depends strongly on the alloying elements. For the Fe-Cr alloys, a model for the formation of the scales, which are characterized by alternating dense and porous layers, is presented. The addition of 5 wt.% Si or Al to Fe-15Cr leads to much better corrosion resistance by the formation of protective Cr_2O_3/Al_2O_3 -layers, however in the case of Al addition the behaviour depends strongly on the experimental conditions, as surface treatment and flow velocity. In Fe-15Cr-10Mo preferential removal of the more reactive metals Fe and Cr was observed resulting in a Mo-enriched porous metal zone underneath the metal-oxide interface. The effect of carbon on the corrosion behaviour was examined by addition of 0.3–0.8 wt.% C to the model alloys. Cr-rich $M_{23}C_6$ -carbides were attacked preferentially while Mo-rich M_6C -carbides are very stable relative to the matrix and the attack occurs in regions surrounding the carbides.

Der Einfluß der Legierungselemente Al, Cr, Mn, Mo, Si und Ti auf das Korrosionsverhalten ferritischer Fe-15Cr-Modellegierungen wurde in einer N_2/He -5 vol.% O_2 Gasmischung mit und ohne Zusatz von 500–1500 vppm HCl bei 600 °C untersucht. Der wesentliche Korrosionsmechanismus ist die „aktive Oxidation“, bei der sich flüchtige Metallchloride an der Metall/Oxid-Grenzfläche bilden. Verdampfen und anschließende Umsetzung der Chloride in Oxide führt zu porösen und schlecht haftenden Oxidschichten. Hohe Massenzunahmen wurden beobachtet bei Fe-15Cr, Fe-35Cr und Fe-15Cr mit Zusätzen von 5 gew.% Ti, 10 gew.% Mn oder 10 gew.% Mo. Die spezifische Morphologie der gebildeten Oxidschichten hängt stark von den jeweiligen Legierungselementen ab. Im Falle der Fe-Cr Legierungen wird ein Modell für die Bildung der Oxidschichten, die aus abwechselnd kompakten und porösen Schichten bestehen, vorgestellt. Der Zusatz von 5 gew.% Si oder Al führt zu stark verbesserten Korrosionswiderständen durch die Bildung von schützenden Cr_2O_3/Al_2O_3 -Schichten; im Falle des Aluminiums ist dies allerdings kritisch abhängig von den experimentellen Bedingungen, wie Oberflächenbearbeitung und Strömungsgeschwindigkeit. Bei Fe-15Cr-10Mo wird eine bevorzugte Reaktion der reaktiveren Metalle Fe und Cr beobachtet, was zu einer Mo-angereicherten porösen Metallzone unterhalb der Metall/Oxid-Grenzfläche führt. Der Effekt von Kohlenstoff auf das Korrosionsverhalten wurde durch Zulegieren von 0,3–0,8 gew.% C zu den Modellegierungen untersucht. Cr-reiche $M_{23}C_6$ -Karbide werden relativ zur Matrix bevorzugt angegriffen, während Mo-reiche M_6C -Karbide sehr beständig sind und der Angriff bevorzugt in den umgebenden Metallbereichen erfolgt.

1 Introduction

Chlorine-induced high temperature corrosion results in degradation of materials used in a number of applications, such as municipal waste incinerators, where HCl is generated from burning PVC, or power plants using chloride bearing coal. In municipal waste incinerators the oxygen content is typically about 5–10 vol.% while HCl is only 500–2500 vppm HCl. In addition to chlorine and oxygen, the corrosion process in incinerators is influenced by other aggressive gases and deposits

of fly ash, which leads to a very complex environment. Investigations on the corrosion mechanisms under simulated waste incineration environments and the improvement of the materials in use is a topical area of research [1, 2]. The specific interaction of chlorine with various alloying elements in steels is not well understood under these conditions.

From the literature it is known that the presence of chlorine causes accelerated attack in oxidizing environments. Investigations on the corrosion behaviour have been performed in chlorine-containing atmospheres at low-oxygen partial pressure as well as at high-partial pressures on several metals and alloys. In studies on iron [3–7] and chromium [5, 8–10] a strong correlation between corrosion mechanism and oxygen/chlorine ratio and temperature was observed. Numerous investigations on the corrosion behaviour of iron-based

* Prof. Dr. H. J. Grabke, Dr. M. Spiegel, Dr. A. Zahs
Max-Planck-Institut für Eisenforschung GmbH,
Max Planck-Straße 1, D-40237 Düsseldorf (Germany)

Table 1. Nominal compositions of the model alloys (in wt.%)**Tabelle 1.** Nominelle Zusammensetzung der Modellierungen (in Gew.%)

Alloy Designation	Cr	Mn	Mo	Ti	Al	Si	C
Fe-15Cr	15	—	—	—	—	—	—
Fe-15Cr-C	15	—	—	—	—	—	0.3
Fe-15Cr-0.8C	15	—	—	—	—	—	0.8
Fe-35Cr	35	—	—	—	—	—	—
Fe-35Cr-C	35	—	—	—	—	—	0.3
Fe-15Cr-10Mn	15	10	—	—	—	—	—
Fe-15Cr-10Mn-C	15	10	—	—	—	—	0.3
Fe-15Cr-10Mo	15	—	10	—	—	—	—
Fe-15Cr-10Mo-C	15	—	10	—	—	—	0.3
Fe-15Cr-5Ti	15	—	—	5	—	—	—
Fe-15Cr-5Ti-C	15	—	—	5	—	—	0.3
Fe-15Cr-5Al	15	—	—	—	5	—	—
Fe-15Cr-5Si	15	—	—	—	—	5	—

alloys conducted in chloridizing and oxidizing atmospheres are found in [11–19].

In spite of the number of studies, the mechanisms of the corrosion processes are not established considering the specific role of the alloying elements. One reason for this is the complexity of the behaviour. In an environment containing both oxygen and chlorine, volatile as well as condensed reaction products are produced. As the number of alloying elements in the materials increases, the behaviour becomes very complex and the specific role of each element is difficult to differentiate.

Most of the observations in literature have been made at temperatures above 600 °C, whereas there are only a few studies in chlorine containing oxidizing atmospheres in the temperature range up to 600 °C. The corrosion behaviour varies significantly with even small changes in temperature due to the large changes of the vapour pressures of the volatile products.

In this study the influence of alloying elements on the corrosion behaviour of iron-chromium alloys was systematically investigated in chlorine containing oxidizing atmospheres typically found in waste-incinerator plants. The base alloy examined was Fe-15Cr, with a chromium concentration close to the minimum concentration needed for the formation of a protective chromium oxide scale in only oxidizing atmospheres. As alloying elements aluminium, chromium, manganese, molybdenum, silicon and titanium were studied. The chemical compositions of the examined materials are presented in Table 1. Detailed information about the corrosion products will be presented and the corrosion mechanisms and kinetics will be discussed.

The role of carbon in the corrosion process in chlorine containing oxidizing atmospheres is not yet well understood. Several studies were done and some authors observed that carbon in alloys appears to accelerate the attack in these environments [20–23]. In this study analysis of carbon rich alloys was undertaken in comparison to low carbon alloys to observe the specific influence of carbon on the corrosion behaviour. Special attention was given to the stabilities of the formed carbides as a function of their chemical composition.

2 Experimental

Exposure tests and thermogravimetric experiments were carried out at 600 °C in a N₂/He-5 vol.% O₂ gas mixture

with and without additions of 500–1500 vppm HCl using the ferritic model alloys listed in Table 1. The alloys were melted in a vacuum induction furnace and exposed in the as cast condition. For the ferritic Fe-15Cr-0.8C alloy heat treatments were conducted in order to establish nearly complete precipitation of the carbides, i.e. homogenized at 1100 °C for 6 days and then sensitized at 750 °C for 48 h. The alloys were cut into 10x10x2 mm specimens, which were ground through 1000 grit SiC and for the thermogravimetric experiments additionally polished with 3 µm diamond suspension. Afterwards the samples were cleaned and degreased with acetone in an ultrasonic bath and subsequently weighed.

In the case of exposure experiments N₂-5 vol.% O₂ and for the thermogravimetric experiments He was used as the carrier gas. For thermogravimetry helium allows a very sensitive measurement free of vibrations and disturbances. Exposures were conducted for 168 hours; thermogravimetric experiments for times up to 176 hours.

Exposure tests were carried out in a horizontal silica tube furnace with a sufficiently large temperature constant zone. The specimens were mounted on a quartz sample holder, which was constructed so that any spalled corrosion products could be isolated and collected for each sample after exposure. Hydrogen chloride was added to the N₂-5 vol.% O₂ mixture by passing parts of the gas mixture through a saturator containing an azeotropic hydrochloric acid solution. All gases were dried by flowing through columns filled with P₂O₅. A total flow velocity of 2.5 ml/s was controlled by capillary flowmeters.

Information about the extent of corrosion is given by the total mass change of the specimens during the corrosion process and by the mass loss after subsequent removal of corrosion products. The corrosion products were removed either by ultrasonic cleaning or by an additional chemical treatment, depending on the morphology and adherence of the products. The chemical treatment was performed by pickling in an alkaline solution of KMnO₄ and inhibited HCl.

For the thermogravimetric experiments samples were suspended inside a vertical furnace at quartz rods connected to a Sartorius continuously recording microbalance. Because of the smaller diameter of the furnace tube (factor two) and the absence of a sample holder the gas velocity is significantly higher than for the exposure experiments and the thickness of the laminar boundary layer is reduced. The significance of this will be discussed in later sections.

After the corrosion experiments the corrosion products and the surfaces of the specimens were examined using Light Optical Microscopy (OM), Scanning Electron Microscopy (SEM), Energy Dispersive Spectroscopy (EDX), X-Ray Diffraction (XRD), X-Ray Photoelectron Spectroscopy (XPS) and Auger Electron Spectroscopy (AES). The analysis of the morphology of the thick and porous corrosion scales was undertaken by preparation of metallographic cross sections. The cross sections were ground and polished dry to prevent dissolution of the formed chlorides.

3 Results and discussion

3.1 Thermodynamic properties and aspects of chlorine induced corrosion

From studies by *Abels et. al.* [24] can be concluded that Cl_2 and not HCl is the main aggressive species in corrosion, at least for short exposure times. In oxidizing atmospheres, chlorine is formed from HCl by the following reaction (Deacon Process):

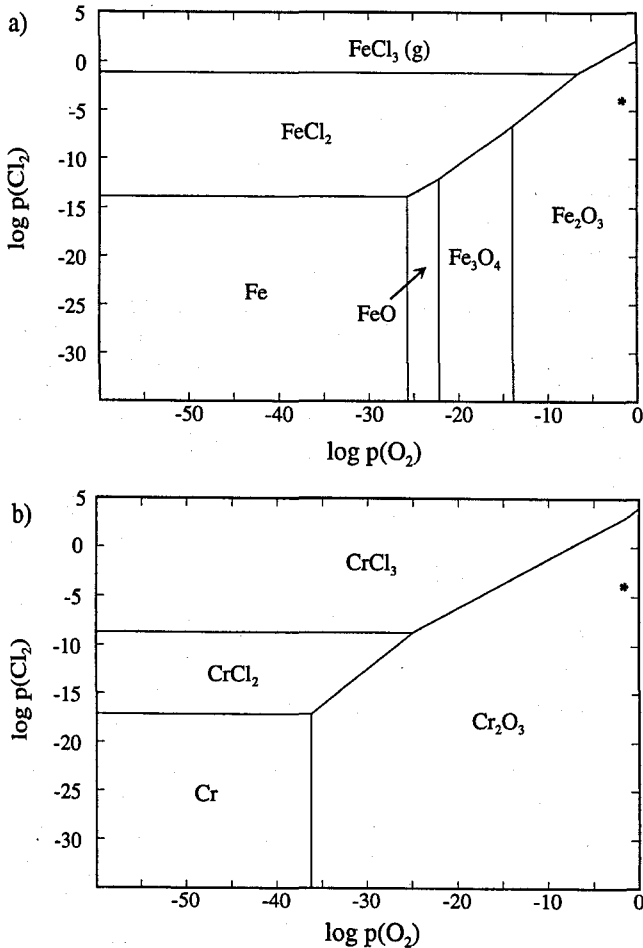
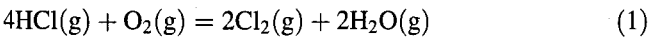
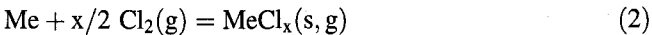


Fig. 1. Thermodynamic stability diagrams of the systems $\text{Fe-O}_2\text{-Cl}_2$ (a) and $\text{Cr-O}_2\text{-Cl}_2$ (b) at 600 °C
Abb. 1. Thermodynamische Stabilitätsdiagramme der Systeme $\text{Fe-O}_2\text{-Cl}_2$ (a) und $\text{Cr-O}_2\text{-Cl}_2$ (b) bei 600 °C

It is important to note that the equilibrium of equation (1) is established very slowly in the gas phase but that metal oxides act as a catalyst for the reaction. Thus it may be assumed that the equilibrium of reaction (1) is approached on and in oxide layers. In the following, Cl_2 is regarded as the active species and the partial pressure of chlorine p_{Cl_2} is determined by the equilibrium condition of reaction (1).

In an oxidizing chlorine-containing atmosphere the thermodynamic stability of metal chlorides and oxides at a given temperature depends on the partial pressures of oxygen and chlorine. The thermodynamic phase stability diagrams for the systems $\text{Fe-O}_2\text{-Cl}_2$ and $\text{Cr-O}_2\text{-Cl}_2$ at 600 °C are shown in Figure 1a and 1b, in which the equilibrium conditions for atmospheres containing 5 vol.% O_2 and 500 vppm HCl are marked. In Table 2 the standard Gibbs free energies of formation for relevant metal chlorides are presented and compared to the values for the metal oxides.

For the activities of Cl_2 and O_2 present in the experiments, the oxides are the thermodynamically most stable phases in equilibrium with the gas phase for all metal species in the studied alloys. At the metal/oxide interface the oxygen partial pressure is low and the chlorides become stable. Depending on the alloying elements several volatile solid and gaseous chlorides can form at the interface, as given in equation (2).



The formed solid chlorides have considerable equilibrium vapour pressures $p_v(\text{MeCl}_x)$ at 600 °C and evaporate continuously according to:



These vapour pressures are presented in Table 3. The chlorides of silicon, aluminium and the higher valent chlorides of molybdenum and titanium have at 600 °C a partial pressure

Table 2. Standard Gibbs free energies of formation of metal chlorides and oxides (kJ/mol) [25]

Tabelle 2. Freie Standard-Bildungsenthalpien für Metallchloride und -oxide (kJ/mol) [25]

Metal	Chlorides		Oxides	
Fe	FeCl_2	− 232,1	Fe_2O_3	− 591,8
	$\text{FeCl}_3(\text{g})$	− 237,1	Fe_3O_4	− 829,7
Cr	CrCl_2	− 286,0	Cr_2O_3	− 908,0
	CrCl_3	− 358,4		
Mn	MnCl_2	− 366,7	Mn_2O_3	− 731,0
			Mn_3O_4	− 1084,5
			MnO	− 321,0
Mo	MoCl_2	− 168,4	MoO_3	− 523,6
	MoCl_3	− 240,9	MoO_2	− 428,0
	$\text{MoCl}_4(\text{g})$	− 296,1		
	$\text{MoCl}_5(\text{g})$	− 287,7		
Ti	TiCl_2	− 374,5	TiO_2	− 784,9
	TiCl_3	− 531,9	Ti_4O_7	− 2854,3
	$\text{TiCl}_4(\text{g})$	− 657,8	Ti_2O_3	− 1274,1
			TiO	− 458,0
Al	$\text{AlCl}_3(\text{g})$	− 541,1	Al_2O_3	− 1401,3
Si	$\text{SiCl}_4(\text{g})$	− 547,3	SiO_2	− 752,4

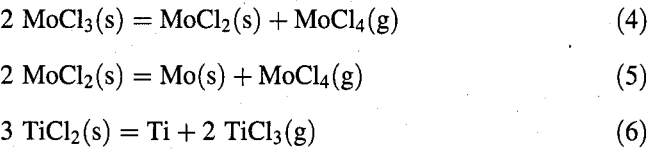
Table 3. Equilibrium vapour pressures of solid chlorides and equilibrium oxygen partial pressures of the reaction from gaseous chloride to solid oxides at 600 °C (in bar) (based on the data in [25, 26])

Tabelle 3. Gleichgewichtspartialdrücke fester Chloride und Gleichgewichts-Sauerstoffpartialdrücke der Reaktion gasförmiger Chloride zu Oxiden bei 600 °C (in bar) (auf der Basis von Daten aus [25, 26])

Chloride	p _v (MeCl _x)	Chloride / Oxide	P _{O2} (500 vppm)	P _{O2} (1500 vppm)
FeCl ₂	1.03 · 10(−3)	FeCl ₂ (g) / Fe ₂ O ₃	1.15 · 10(−10)	4.97 · 10(−10)
FeCl ₃ (g)	(g)	FeCl ₃ (g) / Fe ₂ O ₃	1.08 · 10(−12)	9.73 · 10(−12)
CrCl ₂	1.76 · 10(−6)	CrCl ₂ (g) / Cr ₂ O ₃	5.56 · 10(−19)	2.41 · 10(−18)
CrCl ₃	8.42 · 10(−5)	CrCl ₃ (g) / Cr ₂ O ₃	1.25 · 10(−14)	1.13 · 10(−14)
MnCl ₂	7.22 · 10(−5)	MnCl ₂ (g) / Mn ₃ O ₄	1.03 · 10(−5)	5.33 · 10(−5)
		MnCl ₂ (g) / Mn ₂ O ₃	1.75 · 10(−5)	7.59 · 10(−5)
MoCl ₂	3.56 · 10(−3)*			
MoCl ₃	0.345*			
MoCl ₄ (g)	(g)	MoCl ₄ (g) / MoO ₂	6.85 · 10(−16)	6.16 · 10(−15)
		MoCl ₄ (g) / MoO ₃	1.20 · 10(−14)	5.21 · 10(−14)
MoCl ₅ (g)	(g)	MoCl ₅ (g) / MoO ₂	3.27 · 10(−18)	5.10 · 10(−17)
		MoCl ₅ (g) / MoO ₃	3.42 · 10(−16)	2.13 · 10(−15)
TiCl ₂	1.26 · 10(−4)**			
TiCl ₃	9.85 · 10(−3)	TiCl ₃ (g) / TiO ₂	2.54 · 10(−21)	1.32 · 10(−20)
TiCl ₄ (g)	(g)	TiCl ₄ (g) / TiO ₂	1.33 · 10(−15)	1.20 · 10(−14)
AlCl ₃ (g)	(g)	AlCl ₃ (g) / Al ₂ O ₃	1.00 · 10(−20)	9.01 · 10(−20)
SiCl ₄ (g)	(g)	SiCl ₄ (g) / SiO ₂	2.87 · 10(−20)	2.58 · 10(−19)

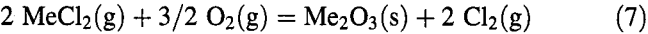
* MoCl₄(g)
** TiCl₃(g)

> 1 atm and will be formed only as gaseous chlorides. In the case of molybdenum and titanium the lower valent chlorides disproportionate into higher valent gaseous chlorides and metal.



In these cases the vapour pressures for the relevant gaseous chlorides MoCl₄ and TiCl₃ are presented in Table 3, which are much higher than the vapour pressures of the lower valent chlorides MoCl₃(g), MoCl₂(g) and TiCl₂(g).

The volatile chlorides evaporate and diffuse towards the gas/scale interface. Within the scale an oxygen partial pressure gradient exists. Upon reaching regions with higher oxygen partial pressures, the evaporating chlorides react with oxygen to form solid oxides releasing chlorine. For a divalent metal chloride converting to a trivalent metal oxide the equilibrium is given by:



The process consisting of the formation of volatile metal chlorides and subsequent oxidation of the evaporating chlorides is called 'active oxidation' [27, 28]. The name is chosen because no passivation by a protective oxide layer occurs but a very loose unprotective scale forms. The equilibrium oxygen partial pressures p(O₂) in several chloride/oxide equilibria, such as Eqn. (7), are also given in Table 3 for the Cl₂-activity of the gas atmosphere (2,31/6,93·10^{−4} bar for 500/1500 vppm HCl) and the equilibrium vapour pressures of the metal chlor-

ides at 600 °C. Chlorides of silicon, aluminium and titanium convert into oxides at very low oxygen pressures, whereas manganese chloride is converted at much higher oxygen pressures. The transformation of the iron chloride FeCl₂ occurs at higher oxygen partial pressures than for CrCl₂, therefore, evaporating chromium chlorides convert into oxides closer to the metal surface than iron chlorides. Evaporating chlorides which are not converted to oxides within the scale are diffusing into the flowing gas leading to a mass loss of the specimen. As it will be shown in section 3.4, active oxidation is the main observed corrosion mechanism and only a few metal chlorides leave the sample by volatilization. Therefore, the observed mass gain corresponds approximately to the extent of corrosion attack.

For the interpretation of the chloride vapour pressures it must be taken into account, that the presented values consider the equilibria of pure metal chlorides. In the case of alloys, however, mixed chlorides form and their vapour pressures can only be estimated from the presented vapour pressures.

3.2 Alloy microstructures and compositions

For a complete understanding of the corrosion behaviour it is of importance to know the microstructure of the alloys. The alloys were investigated by Light Optical Microscopy (metallographically polished and etched samples; etchants: V2A and Murakami) and XRD analysis. The phase compositions were determined by the computer program Thermo-Calc [29]. Except for Fe-15Cr-0.8C, the alloys are used in the as-cast condition, characterized by large grain sizes. For Fe-15Cr, Fe-35Cr, Fe-15Cr-10Mo, Fe-15Cr-5Al and Fe-15Cr-5Si single phase ferritic microstructures were observed. Manganese is known as an austenite stabilizer, accordingly in Fe-15Cr-

10Mn small austenitic precipitates were found within the ferrite. Fe-15Cr-5Ti also consists of two phases, ferrite and an intermetallic compound, which from thermodynamic considerations is expected to be $\text{Cr}_6\text{Fe}_{18}\text{Ti}_5$ [30]. Unfortunately no XRD reference data is available, but analysis carried out with EDX shows a good correspondence to that composition.

For the carbon containing alloys the formation of different types of carbides is expected from thermodynamic calculations. In Fe-15Cr-0.3C only very small carbides locally precipitated, and a complex multiphase microstructure of ferrite, martensite and chromium rich carbides was observed. In the heat treated Fe-15Cr-0.8C alloy, very fine carbides were found evenly distributed throughout the metal phase with minor enrichments at the grain boundaries. The carbides were identified as chromium rich M_{23}C_6 by XRD analysis. In Fe-35Cr-C the precipitated M_{23}C_6 carbides (XRD) are elongated in appearance and often contain a core of the base metal. The equilibrium chromium content of these carbides, 84.2 wt.%, is greater than for the carbides in Fe-15Cr-0.8C (72.8 wt.%) at 600 °C. For Fe-15Cr-10Mn-C the matrix is mainly austenitic with only small areas of ferrite, because the higher carbon content stabilizes the γ -phase, and only very small precipitates of carbides were observed. For Fe-15Cr-10Mo-C molybdenum rich M_6C carbides were detected by XRD analysis. Two morphologies of M_6C carbides were observed: globular (2–3 μm diameter) and elongated (> 20 μm in length and 1–2 μm in width). In thermodynamic equilibrium these carbides would be only stable at temperatures above 750 °C and have a molybdenum content of 51.0 wt.% at 1200 °C. As expected from thermodynamic considerations globular TiC carbides (1–4 μm in size) were observed in Fe-15Cr-5Ti-C, which are preferentially but not exclusively located along grain boundaries. All present carbides are too small for quantitative analysis by EPMA for which a particle diameter of at least 5 μm is necessary.

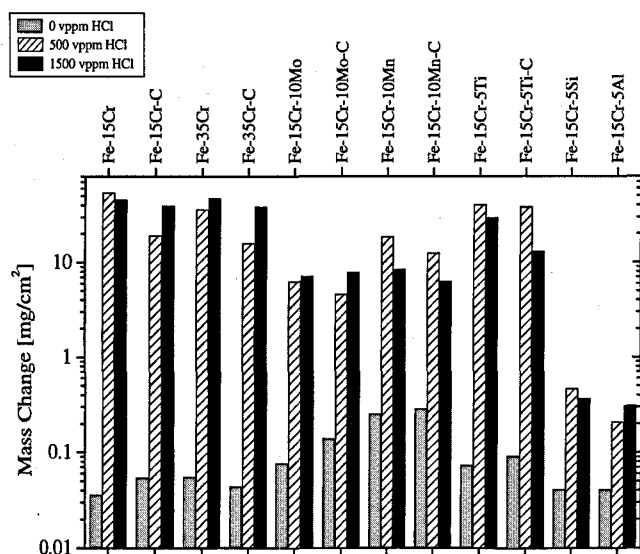


Fig. 2. Mass change of the model alloys after 168 h of exposure in N_2 -5% O_2 (0–1500) vppm HCl at 600 °C presented in a logarithmic plot

Abb. 2. Logarithmische Auftragung der Massenänderung der Modelllegierungen nach 168 h Auslagerung in N_2 -5% O_2 (0–1500) vppm HCl bei 600 °C

3.3 Oxidation behaviour of the alloys

Figure 2 shows a logarithmic plot of mass changes of the alloys observed after 168 h of exposure in N_2 -5% O_2 with additions of 0, 500 and 1500 vppm HCl at 600 °C. In the atmosphere without chlorine in most cases protective oxide scales formed and small mass gains were found, whereas much larger mass gains were observed for the chlorine containing atmospheres. For example, in the case of the base alloy Fe-15Cr, the addition of chlorine increases the mass gain by a factor of about thousand.

After 168 h of oxidation in N_2 -5% O_2 mainly protective oxides scales formed, which were investigated with SEM and analyzed by AES sputter profiles, EDX and XRD. Due to the small thickness of the oxide scales AES and XRD are the more suitable analysis methods.

3.3.1 Fe-15Cr/Fe-35Cr

The iron chromium alloys Fe-15Cr and Fe-35Cr with and without carbon form protective chromium oxide layers. Fig 3a shows an AES sputter profile of the oxide scale on Fe-15Cr. The relatively small amount of chromium in the alloy is obviously sufficient for the formation of a protective Cr_2O_3 layer, which has a thickness of about 0.2 μm . The addition of 0.3 wt.% carbon to Fe-15Cr and Fe-35Cr had no significant influence on the formation of chromia.

More detailed investigations on the effect of chromium rich carbides in oxidizing atmospheres have been performed by Durham et al. [31], who studied a number of steels with chromium carbides oxidized at 850 °C in pure oxygen. They found that for a fine distribution of carbides in an austenitic matrix or any type of distribution of chromium carbides in a ferritic matrix, the chromium in the carbides acts as a reservoir for growth of a continuous chromium oxide layer with a resultant sub-surface carbide dissolution zone. Under these corrosion conditions, the chromium rich carbides aid in the formation of a continuous protective chromium oxide layer.

3.3.2 Fe-15Cr-10Mo

The AES sputter profile of Fe-15Cr-10Mo is presented in Fig. 3b. A protective Cr_2O_3 layer without any enrichment of molybdenum is formed. The thickness of the scale is 0.6 μm , which is three times thicker than in the case without addition of molybdenum.

3.3.3 Fe-15Cr-10Mn

On Fe-15Cr-10Mn a nonprotective Mn_2O_3 layer is formed. The corrosion scale appears grey and is much thicker than the protective Cr_2O_3 layers, corresponding to the observed higher mass gains. For this reason, no AES sputter profile of the complete scale was recorded. In contrast to the chromia layers the oxide layer is poorly adherent and partially spalls from the surface. By XRD analysis mainly Mn_2O_3 and small amounts of Fe_2O_3 and Cr_2O_3 were detected. In an AES sputter profile of the outer part of the scale only manganese and oxygen were found. The general corrosion behaviour of the austenitic Fe-15Cr-10Mn-C was very similar, but on the surface of the corrosion layer a higher chromium content was found by EDX analysis.

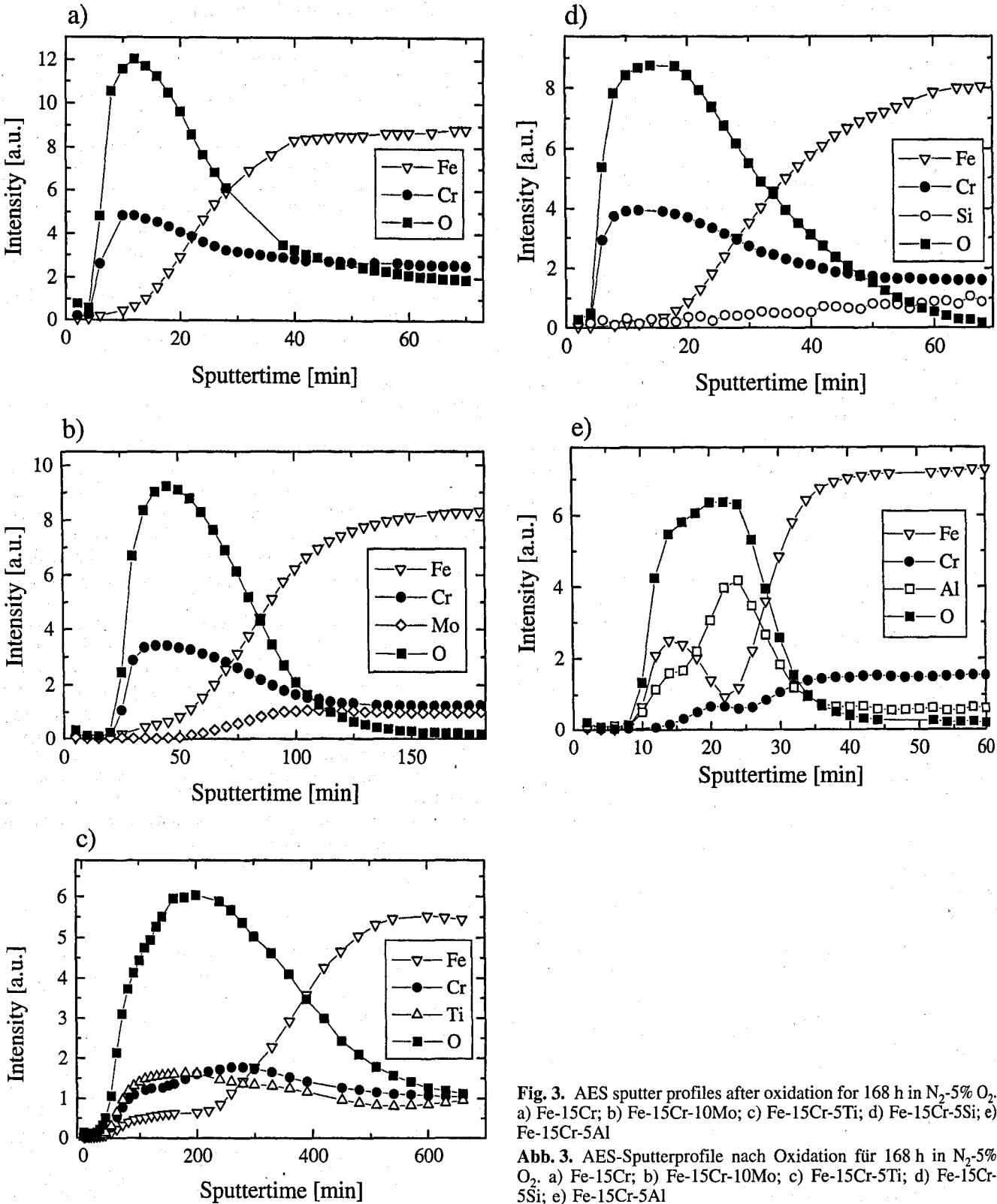


Fig. 3. AES sputter profiles after oxidation for 168 h in N₂-5% O₂. a) Fe-15Cr; b) Fe-15Cr-10Mo; c) Fe-15Cr-5Ti; d) Fe-15Cr-5Si; e) Fe-15Cr-5Al

Abb. 3. AES-Sputterprofile nach Oxidation für 168 h in N₂-5% O₂. a) Fe-15Cr; b) Fe-15Cr-10Mo; c) Fe-15Cr-5Ti; d) Fe-15Cr-5Si; e) Fe-15Cr-5Al

3.3.4 Fe-15Cr-5Ti

Fig. 3c shows the AES sputter profile of Fe-15Cr-5Ti. A relatively thick and well adherent oxide layer containing titanium, chromium and a small amount of iron is formed. The outer region is enriched in titanium while the inner region is enriched in chromium. The iron content is nearly constant throughout the scale.

3.3.5 Fe-15Cr-5Si

The promoting effect of silicon on the formation of protective Cr₂O₃ scales was found in a number of studies, where mainly two possible mechanisms are discussed. The first is the formation of a thin silica layer under the chromia scale, acting as a diffusion barrier and slowing down the rate of alloy oxidation. Wood et al. observed such an effect in Fe-Cr-

alloys at high temperatures in the range of 1000–1300 °C [32]. The other mechanism discussed is that the addition of silicon increases the diffusion of chromium in the alloy, an influence which has not yet been proven for ferritic iron chromium alloys. In austenitic alloys Si has an accelerating influence on the diffusion of chromium [33].

Fig. 3d shows an AES sputter profile of the protective chromia layer on Fe-15Cr-5Si. The scale, with a thickness of 0.25 µm, is insignificantly thicker than in the case without addition of silicon. No silicon enrichment was detected at the metal/scale interface.

3.3.6 Fe-15Cr-5Al

In Fig. 3e the sputter profile of the scale formed on Fe-15Cr-5Al is presented. From X-ray diffraction, Fe₂O₃ and γ-Al₂O₃ were the phases detected. The oxide scale is very thin and protective. In the outer scale an iron-rich oxide has formed, containing significant amounts of aluminium. The inner scale consists mainly of Al₂O₃ with small concentrations of iron and chromium. Small local enrichments of Fe₂O₃ are found distributed over the surface of the oxide layer.

3.4 Corrosion in N₂-5 % O₂-HCl

3.4.1 Iron chromium alloys (Fe-15Cr, Fe-35Cr)

As shown in Fig. 2, the iron chromium alloys Fe-15Cr and Fe-35Cr exhibit the highest corrosion rates compared to the other alloys in atmospheres containing 500 and 1500 vppm HCl. The different HCl contents had no significant effect on the observed mass gains. A comparison of the mass gains of Fe-15Cr and Fe-35Cr shows that the increased chromium content does not lead to better corrosion resistance, a striking result. Accordingly in the following the chromium content in the matrix and HCl content in the atmosphere will only be considered when differences are found.

The corroded specimens are covered with a very thick, porous and grey-coloured scale. The scales are very poorly adherent at the metal/scale interface and easily spall. Fig. 4a shows a micrograph of a metallographic cross section of the corrosion scale on Fe-15Cr, whereas in Fig. 4b a micrograph of the oxide scale surface is presented. The thickness of the scale is more than 1 mm. Alternating very porous and more compact oxide layers are visible (Fig. 4a, c, d). Components of the oxide layer are Fe₂O₃, Cr₂O₃ and small amounts of Fe(Fe,Cr)₂O₄ spinel, as detected by XRD. The proportion of chromium in the scale corresponds to the amount of chromium in the metal.

At the oxide/metal interface the oxygen pressure is low and mixed iron/chromium chlorides are formed. From the phase diagram of FeCl₂ and CrCl₂ [34] it can be seen that the chlorides are completely miscible at 600 °C. Fig. 4e shows a micrograph of typical (Fe, Cr)Cl₂ chlorides on the metal surface after removal of the external corrosion scale. The chromium content of the chlorides was determined by EDX analysis and corresponds well with the chromium content in the metal. The part of Cr in the chlorides on Fe-15Cr was 10–20 % and on Fe-35Cr 25–40 %. Typical attack of the matrix surface with chloride formation is shown in a cross section in Fig. 4f. The chloride formation occurs preferentially along the grain boundaries on the metal surface leading to grain boundary etching (Fig. 4g).

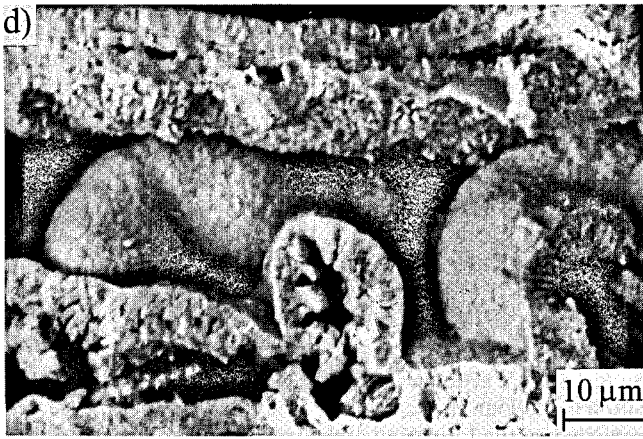
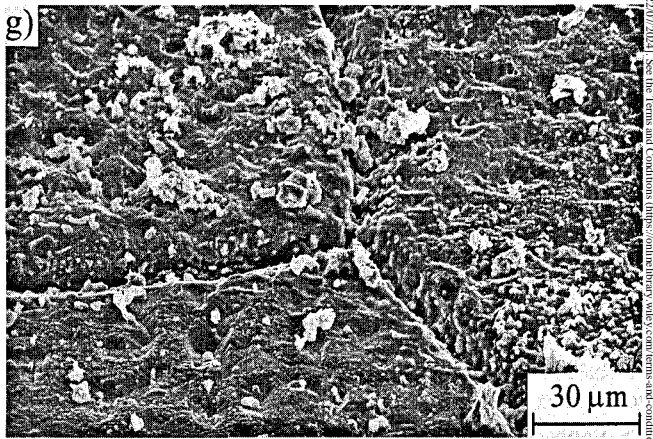
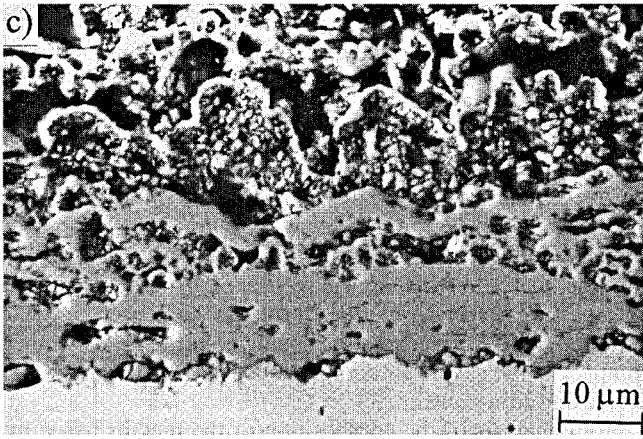
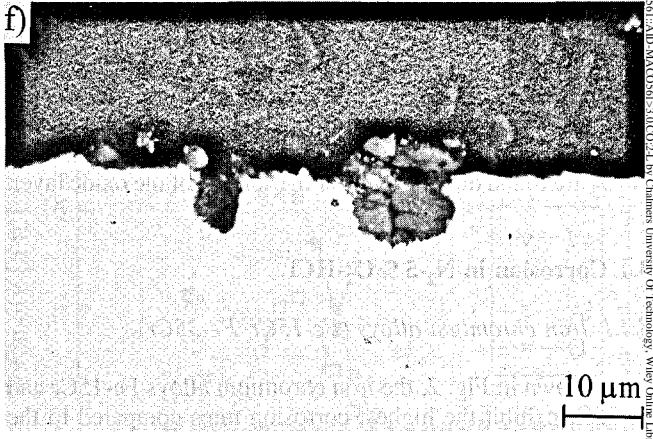
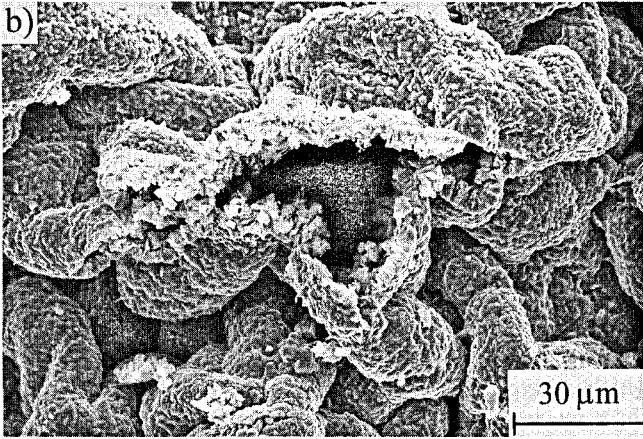
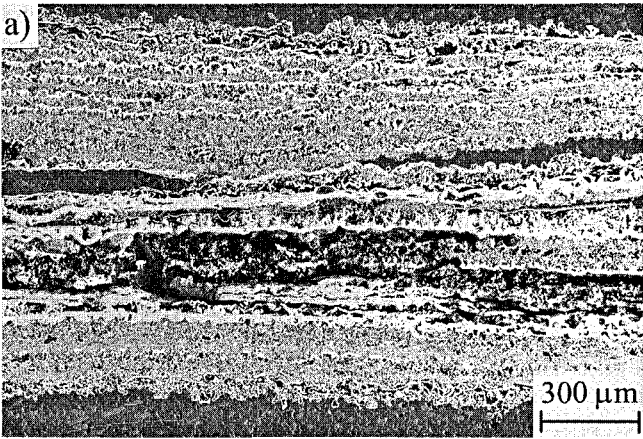
Fig. 5 provides a schematic model of the formation of the oxide scale, which consists of more compact layers and porous bubbly zones. In the initial stage both oxides and chlorides are formed on the alloy surface (Fig. 5a) [35]. Evaporation of volatile chlorides is indicated by arrows. The formed volatile chlorides are not stable in contact with the gas and react with oxygen under formation of oxides. A friable oxide layer forms which is full of cracks and pores. Evaporating metal chlorides diffuse outwards through the cracks and pores and convert into solid oxides in regions of higher oxygen pressure (Fig. 5b) or are removed by the gas flow. The oxides formed from chlorides are hollow and bubble shaped. Growth stresses and the presence of chlorides on the metal surface lead to poorly adherent scales which spall locally during the corrosion process, but remain in contact with the specimen. Then the gas phase can easily reach the metal surface again and new scale formation starts from the beginning as already described (Fig. 5c). Free spaces between two compact oxide layers are partially filled by oxides formed by evaporating chlorides. This procedure continues (Fig. 5d) and leads to the observed alternating morphology of the oxide scale.

Characteristic features of the presented mechanism can be seen in the micrographs Fig. 4a–d. A top view of the bubble-shaped iron rich oxides is shown in Fig. 4b. More details of the morphology of these oxides can be seen in metallographic cross sections (Fig. 4c and d). In Fig. 4d, the crystalline inner structure of the oxide bubbles can be seen and the more compact oxide layer above. The surfaces of the oxides formed by active oxidation are very often covered with Fe₂O₃-whiskers, which is a typical morphology for oxides formed from the gas phase by chemical transport reactions. Near the oxide/gas interface, the bubble shaped oxides consist mainly of iron oxide, but the chromium content increases closer to the metal/oxide interface, because gaseous chromium chlorides are converted earlier and at smaller oxygen partial pressures than the gaseous iron chlorides. This is consistent with the thermodynamic considerations presented in section 3.1. Also in the more compact oxide layers the chromium contents increase going from the outer regions inwards.

For the interpretation of the cross sections it must be taken into account that the free spaces within the porous layers are partly filled with small oxide particles from the grinding process and, therefore, the porous layers appear to be more dense than they are in fact. The higher chromium content in Fe-35Cr does not change the general mechanism, but leads to thinner compact oxide layers in comparison to Fe-15Cr due to the decreasing iron content.

From analysis of the composition of the metal surface by EDX no depletion of iron or chromium was detected. The formation of the mixed (Fe,Cr)Cl₂ chlorides leads to a homogeneous attack of the matrix. Due to the formation of the chlorides at the metal/oxide interface and their high vapour pressures, no formation of a protective Cr₂O₃ layer occurs at 600 °C.

Fig. 6a shows the thermogravimetric results obtained in He-5% O₂-500 vppm HCl for Fe-15Cr and Fe-35Cr in comparison to Fe-15Cr-5Ti. The kinetics are characterized by frequent spalling of the oxide layers from the surface, corresponding to irregular mass gains. Spalling of an oxide layer leads to an acceleration of the corrosion process and is indicated as a new ascent of the curve. With the formation of a new layer the rate of the mass gain again decreases. The overall kinetic curves show a sequence of stages with nearly parabolic oxidation behaviour. In the beginning of the corrosion process the frequency of the formation of the single oxide layers is so high



◀ **Fig. 4.** SEM micrographs of corroded Fe-Cr specimens after 168 h exposure in N₂-5% O₂ (500–1500) vppm HCl. a) Cross section of the entire corrosion scale formed on Fe-15Cr. b) Oxides on the surface of the corrosion layer on Fe-15Cr formed by conversion of evaporating chlorides. c) Cross section of the inner part of the corrosion layer on the metal surface of Fe-35Cr. d) Details of the oxide morphology in a cross section of the corrosion layer of Fe-15Cr. e) (Fe, Cr)Cl₂-crystals on the metal surface of Fe-35Cr. f) Typical local attack of the metal by chlorides in a cross section of Fe-15Cr. g) Grain boundaries on the surface of Fe-35Cr after removal of the corrosion scale (tilted at 45° from horizontal)

Abb. 4. REM-Bilder von korrodierten Fe-Cr-Proben nach 168 h Auslagerung in N₂-5% O₂ (500–1500 vppm HCl). a) Querschliff der gesamten Korrosionsschicht von Fe-15Cr. b) Oxide auf der Oberfläche der Korrosionsschicht von Fe-15Cr, gebildet durch Oxidation gasförmiger Metallchloride. c) Querschliff des inneren Teils der Korrosionsschicht auf der Metalloberfläche von Fe-35Cr. d) Details der Oxidmorphologie in einem Querschliff der Korrosionsschicht auf Fe-15Cr. e) (Fe, Cr)Cl₂-Kristalle auf der metallischen Matrix von Fe-35Cr. f) Typischer lokaler Angriff der Metalloberfläche durch Chloride in einem Querschliff von Fe-15Cr. g) Korngrößen auf der Oberfläche von Fe-35Cr nach Entfernen der Korrosionsschicht (um 45° aus der Horizontalen gekippt)

that the overall reaction rate is approximately linear with time. In Fig. 6b a closer look at the kinetics in the linear regime is presented, showing the periodic fluctuations. As corrosion proceeds, the total corrosion scale gets thicker and denser leading to a decrease of the total mass gain per time, but a stable situation without the possibility of further spalling of the oxide layer is not reached. The thermogravimetric results are in good agreement with the corrosion mechanism presented above.

In the thermogravimetric experiments the corrosion layer formed on Fe-15Cr is more compact and consists of only a few different oxide layers, whereas the corrosion scale on Fe-35Cr shows the same multilayered morphology as in the exposure experiments. Due to the higher gas velocity at the boundary layer the chlorides are converted into oxides more distant from the metal surface and therefore less growth stresses appear promoting better adherence of the scale. With increasing chromium contents the amount of chlorides which are converted into oxides at very small oxygen pressures increases, and a similar scale morphology is observed as in the exposure experiments. The observation that a higher gas velocity is promoting the formation of denser iron rich oxide layers was also made in the case of Fe-15Cr-10Mo.

3.4.2 The effect of molybdenum (Fe-15Cr-10Mo)

The addition of 10 weight percent molybdenum leads to an improvement of the corrosion resistance in comparison to Fe-15Cr. The corrosion behaviour is similar in atmospheres with additions of 500 and 1500 vppm HCl, the increase in mass gain with increased HCl content is small (Fig. 2). Fig. 7 shows a cross section of the corrosion scale on Fe-15Cr-10Mo after exposure in an atmosphere containing 1500 vppm HCl. The count rates for the EDX-signal of the metal species within this scale are presented in a linescan in Fig. 8a. The outer part of the oxide scale consists of Fe₂O₃ and Cr₂O₃, whereas no molybdenum was found in this outer region. Compared with the pure iron chromium alloys the scale is more

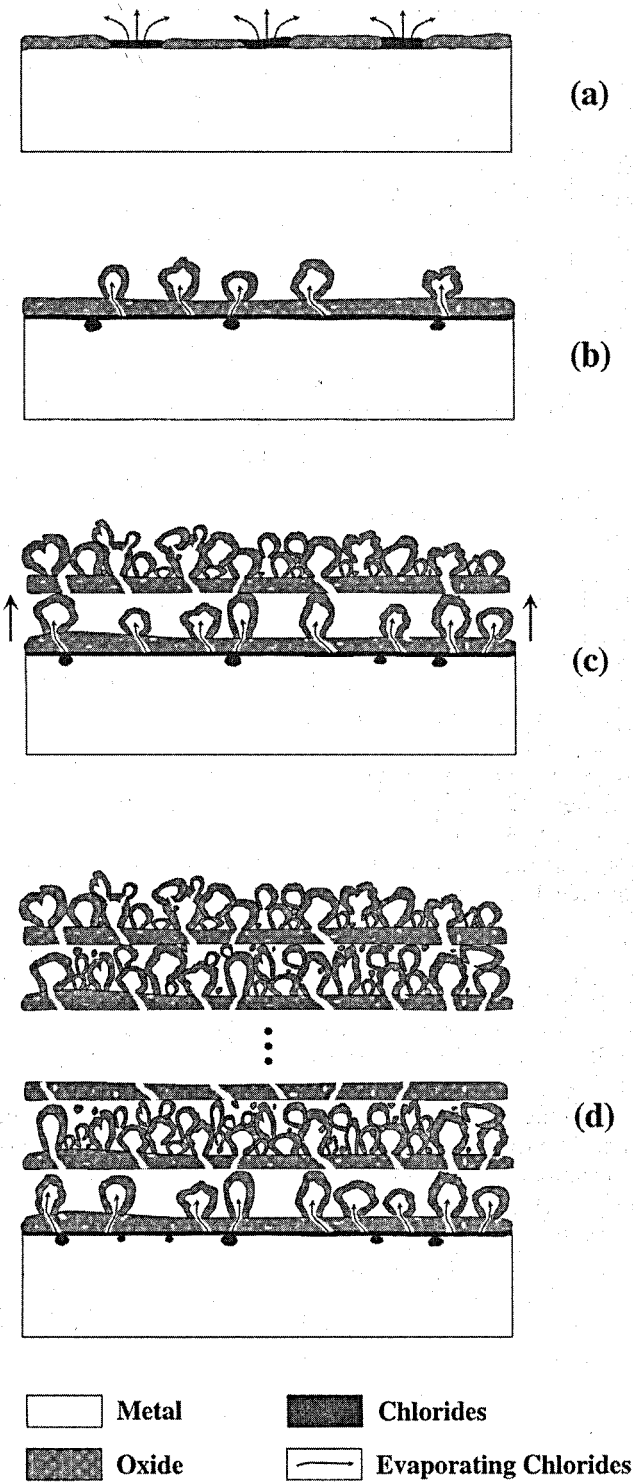


Fig. 5. Schematic model of the corrosion mechanism for Fe-Cr alloys in N₂-5 % O₂-(500–1500) vppm HCl at 600 °C

Abb. 5. Schematisches Modell des Korrosionsmechanismus für Fe-Cr-Legierungen in N₂-5 % O₂-(500–1500) vppm HCl at 600 °C

compact and consists of fewer layers, corresponding to the smaller mass gain. Within the layers an increasing content of chromium is found in the EDX linescan towards the metal/scale interface as also observed in the case of Fe-Cr alloys. At the bottom of the corrosion scale a molybdenum-rich layer with a thickness of about 2 µm was found.

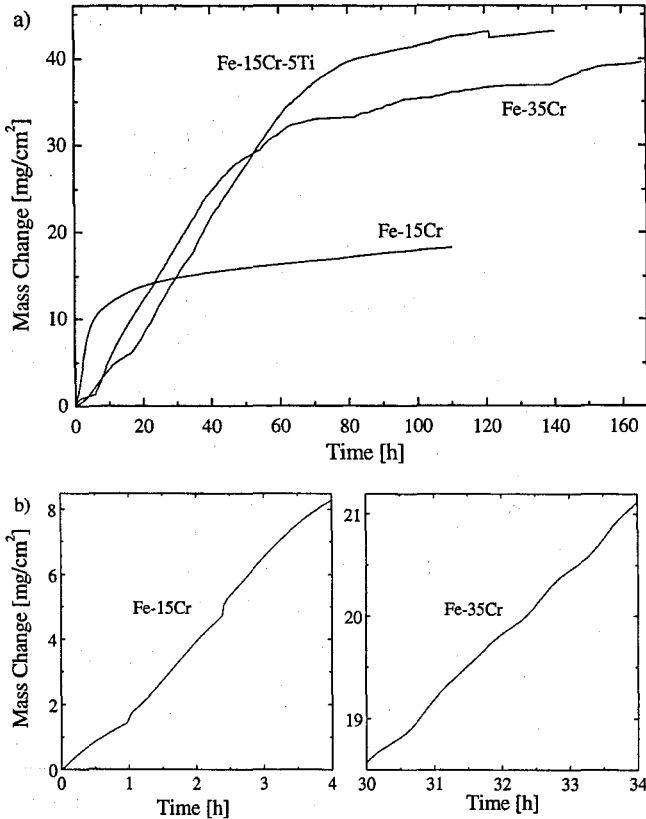


Fig. 6. a) Results of the thermogravimetric experiments for Fe-15Cr, Fe-35Cr and Fe-15Cr-5Ti in He-5 % O₂-500 vppm HCl. b) Details of the thermogravimetric curves for Fe-15Cr and Fe-35Cr in He-5% O₂-500 vppm HCl

Abb. 6. a) Ergebnisse der thermogravimetrischen Experimente für Fe-15Cr, Fe-35Cr und Fe-15Cr-5Ti in He-5 % O₂-500 vppm HCl. b) Ausschnitte der thermogravimetrischen Kurven von Fe-15Cr und Fe-35Cr in He-5 % O₂-500 vppm HCl

Underneath the oxide scale a chromium- and iron-depleted zone of 5 μm thickness has formed in the metal, where molybdenum is significantly enriched. This zone is very porous and the gas phase can easily penetrate to the unaffected metal, as can be seen in a REM-micrograph of a cross section of Fe-

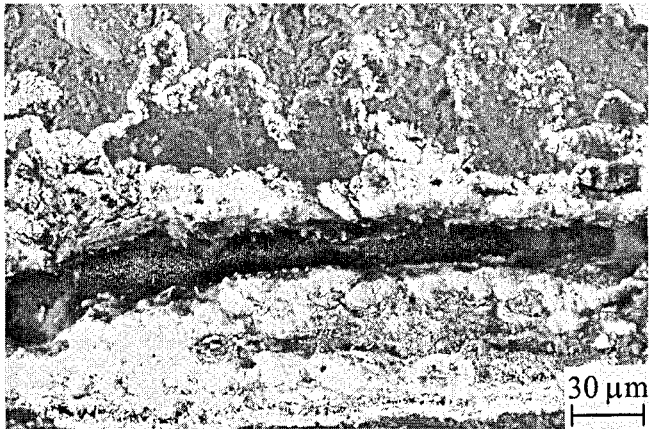


Fig. 7. SEM micrograph of a cross-section of the corrosion scale formed on Fe-15Cr-10Mo after 168 h of exposure in N₂-5 % O₂-1500 vppm HCl

Abb. 7. REM Aufnahme eines Querschliffes der Korrosionsschicht von Fe-15Cr-10Mo nach 168 h Auslagerung in N₂-5 % O₂-1500 vppm HCl

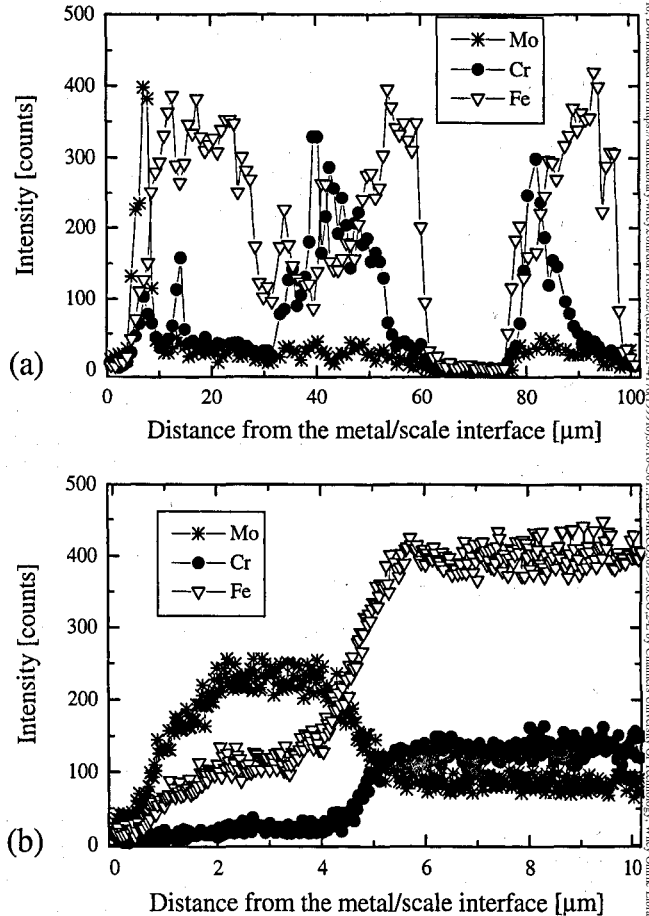


Fig. 8. EDX linescans of Fe-15Cr-10Mo after 168 h of exposure in N₂-5 % O₂-1500 vppm HCl. a) Through the corrosion scale presented in Fig. 7. b) Through the metal region near the surface as shown in Fig. 18

Abb. 8. EDX-Linescans von Fe-15Cr-10Mo nach 168 h Auslagerung in N₂-5 % O₂-1500 vppm HCl. a) Durch die in Abb. 7 dargestellte Korrosionsschicht. b) Durch den Metallbereich an der Oberfläche wie in Abb. 18 abgebildet

15Cr-10Mo-C in Fig. 18a. An EDX linescan through this region into the metal is shown in Fig. 8b. Considering the fact that no adherent oxide scale has formed on the metal substrate the preferential reaction of iron and chromium takes place mainly under formation of volatile metal chlorides, which are converted to oxides close to the metal surface. Small amounts of chlorine were detected near the reaction front within the metal, whereas no oxygen was found within the porous metal zone. On the metal surface beneath the corrosion scale solid (Fe,Cr)Cl₂ chlorides with some Mo were found. The preferential attack of chromium and iron is caused by the higher thermodynamic stability of chromium and iron chlorides in comparison to molybdenum chlorides (Tab. 2).

The corrosion mechanism is typical for the preferential removal of the more reactive metals from an alloy, as *Pickering* observed on Co-Pt and Fe-Pt-alloys in HCl-H₂ gas-mixtures at 1000 K [36]. The morphology of the resulting Pt-enriched metal scales was similar to the morphology of the molybdenum-enriched porous metal scale of Fe-15Cr-10Mo.

A more detailed investigation of the molybdenum enriched layer at the bottom of the corrosion scale was carried out in order to clarify the exact phase composition. From EDX and Auger analysis, molybdenum, iron, chromium and oxygen

were the detected elements. XRD analysis of the bottom of the spalled corrosion layer identified only Fe_2O_3 and Cr_2O_3 , but the intensity of the signal was not sufficient to determine any Mo-containing phase. From XPS analysis of the molybdenum enriched layer it can be concluded that different chemical states of Mo are present. By separation of the peaks and determination of the exact peak positions, detailed information of the chemical states can be obtained [37]. Due to the extreme peak positions, Mo as metal and most likely Mo in MoO_3 were identified, but it is also clear that at least two other Mo containing oxides are present, which could not be clearly identified, because there are so many different molybdenum oxides with similar peak positions.

The corrosion products indicate that the molybdenum-rich layer on the bottom of the corrosion scale is formed under participation of MoCl_2 and MoCl_3 . At the metal/oxide interface, where the molybdenum activity is high due to the depletion of chromium and iron, the formation of lower valent MoCl_2 or MoCl_3 chlorides is expected from thermodynamic calculations. The chlorides disproportionate according to Eqns. (4) and (5) into Mo-metal and gaseous MoCl_4 which is easily converted into molybdenum oxide (Tab. 3) according to its low stability in O_2 -containing gases. Depending on the local oxygen partial pressures, various molybdenum oxides are expected to form. The observation of metallic molybdenum and different types of molybdenum oxides by XPS, and the fact that the reaction products are only observed at the metal scale interface, indicate the presented mechanism.

In Fig. 9 the thermogravimetric results for Fe-15Cr-10Mo are shown. In the beginning a large mass gain occurs by the preferential reaction of iron and chromium. After about 5 hours the mass gain abruptly decreases, most likely due to the enrichment of molybdenum in the near surface region and formation of the partially oxidized molybdenum enriched corrosion layer. After 50 h a further increase of the corrosion rate occurs, because no protective condition is established. Comparing the corrosion products from the exposure tests with that from the thermogravimetric experiments, more compact scales were found at the higher gas velocity and in some regions locally very thin oxide layers were observed.

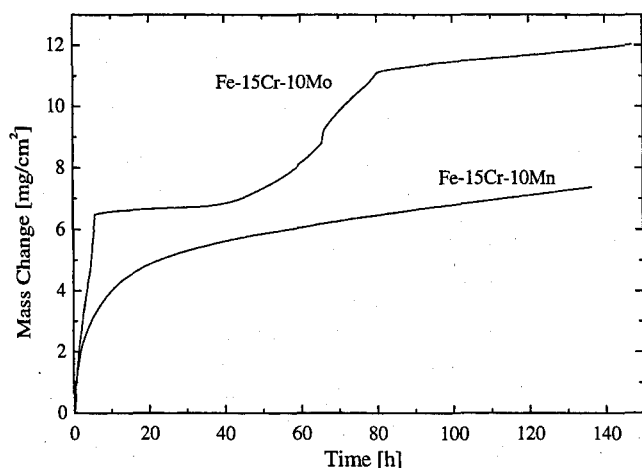


Fig. 9. Thermogravimetric results for Fe-15Cr-10Mo and Fe-15Cr-10Mn in He-5% O₂-500 vppm HCl

Abb. 9. Thermogravimetrische Ergebnisse für Fe-15Cr-10Mo und Fe-15Cr-10Mn in He-5 % O₂-500 vppm HCl

3.4.3 The effect of manganese (Fe-15Cr-10Mn)

As in the case of the molybdenum addition, the addition of manganese leads to an increase of the corrosion resistance of Fe-15Cr (Fig. 2), but the effect of manganese is very different in comparison to molybdenum. On Fe-15Cr-10Mn a thick and better adherent oxide layer is formed, which is shown in a cross sectional micrograph in Fig. 10a. No spalling of the scale occurs during the corrosion process. The outer part of the scale is very compact, but with a wavy morphology, whereas underneath this layer a lot of pores and free spaces are visible. From XRD analysis Fe_2O_3 , Mn_2O_3 and Cr_2O_3 were detected. Cubic crystals of Mn_2O_3 were observed on the surface of the oxide layer (Fig. 10b), since manganese chlorides are converted into oxide at relatively high oxygen partial pressures (Tab. 3). In general, manganese is very reactive such as iron and chromium.

On the metal surface more chlorides were found than on the other investigated alloys. For atmospheres containing 500 vppm HCl, mixed (Mn,Cr,Fe)-chloride particles were formed (Fig. 10c), while for 1500 vppm HCl a dense layer of CrCl_2 was observed (Fig. 10d). From the significantly smaller mass gain for 1500 vppm HCl (Fig. 2) it can be concluded, that the CrCl_2 layer has a protective influence on the corrosion process. The increased formation of the solid chlorides is probably correlated with the formation of the very dense outer oxide layer, which is not formed in this way on the iron chromium alloys. The oxygen partial pressure in the area between this layer and the metal must be low because the gas atmosphere cannot easily diffuse through the compact scale. In addition oxygen is consumed underneath this scale by the active oxidation process, whereas chlorine is not consumed, because it has a catalytic influence on the active oxidation and is released again. By comparison of Fe-15Cr-10Mn and Fe-15Cr-10Mn-C no significant differences were observed.

The kinetics of the corrosion process are nearly parabolic with no indication of spalling of the scale as seen in Fig. 9.

3.4.4 The effect of titanium (Fe-15Cr-5Ti)

The addition of titanium does not lead to a significant improvement in corrosion resistance (Fig. 2). The general corrosion mechanism is the same as presented for the iron-chromium alloys. A micrograph of the complete corrosion scale is presented in Fig. 11a. Alternating dense and porous oxide layers are again formed, such as on the Fe-Cr alloys, in this case with a relatively high thickness of the compact layers. In Fig. 11b a more detailed view of the alternating oxide morphologies is given. A typical hollow iron rich oxide grown over a crack of a compact oxide scale, as presented schematically in Fig. 5b, can be seen in Fig. 11c. Within the compact layers iron oxide was found in the outer part, whereas in the inner part enrichments of chromium and titanium oxide were observed.

The metal is attacked by the formation of mixed (Fe,Cr,Ti)Cl₂ chlorides. In Fig. 11d a cross section of the sample after removal of the corrosion scale is shown. Here it can be seen that the light regions, the titanium-rich intermetallic phase Cr₆Fe₁₈Ti₅, are attacked preferentially. According to the high negative free energies of formation of its chlorides and oxides (Tab. 2), titanium is very reactive in this atmosphere.

Since the corrosion mechanism and the scale morphology are very similar to that of Fe-Cr alloys, the kinetics of the corrosion process are also very similar as shown in Fig. 6a.

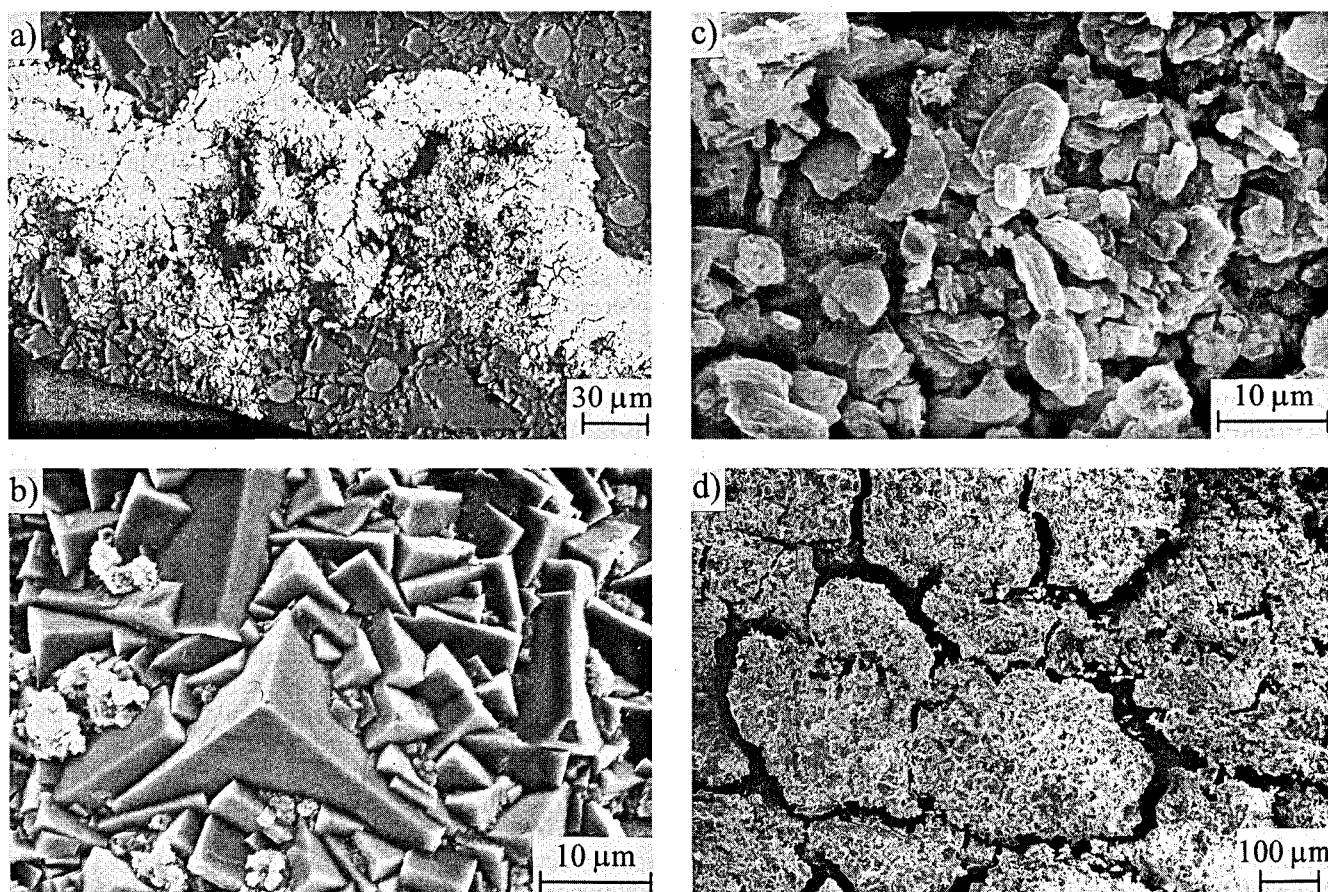


Fig. 10. SEM micrographs of corroded Fe-15Cr-10Mn specimens after 168 h exposure in N_2 -5 % O_2 -(500–1500) vppm HCl. a) Cross section of the corrosion layer (1500 vppm HCl). b) Cubic Mn_2O_3 -crystals on the surface of the corrosion scale (500 vppm HCl). c) Chloride crystals containing Fe, Cr and Mn on the bottom of the corrosion layer (500 vppm HCl). d) $CrCl_2$ -layer on the metal surface (1500 vppm HCl)

Abb. 10. REM Aufnahmen von korrodierten Fe-15Cr-10Mn Proben nach 168 h Auslagerung in N_2 -5 % O_2 -(500–1500) vppm HCl. a) Querschliff der Korrosionsschicht (1500 vppm HCl). b) Kubische Mn_2O_3 -Kristalle auf der Oberfläche der Korrosionsschicht (500 vppm HCl). c) Fe, Cr und Mn enthaltende Chloridkristalle auf der Unterseite der Korrosionsschicht (500 vppm HCl).

d) $CrCl_2$ -Schicht auf der Metall-Oberfläche (1500 vppm HCl)

3.4.5 The effect of silicon (Fe-15Cr-5Si)

On Fe-15Cr-5Si a nearly protective oxide scale forms and detrimental growth of iron rich oxides by active oxidation occurs only locally for 500 vppm HCl as well as for 1500 vppm HCl. The corrosion resistance is strongly improved by the addition of silicon. A cross section of a sample including the entire corrosion scale is shown in Fig. 12. The main part of the oxide scale is separated from the surface due to the preparation process. From XRD analysis Cr_2O_3 and Fe_2O_3 were found as the phases present in the scale. An EDX line-scan of the metal intensities through the scale and the metal surface is presented in Fig. 13. A chromia enriched layer is found on the metal surface which is obviously well adherent, as only the iron rich outer part of the scale was lifted from the surface. A chromium depleted zone below the metal surface was observed, which is an indication of improved chromium diffusion in the ferrite. No enrichment of Si was detected beneath the chromia layer. In the thermogravimetric curve it can be seen that the mass gain is very irregular (Fig. 14), due to the observed local active oxidation. The total mass gain is low but frequent temporary increases of the mass gain are visible.

3.4.6 The effect of aluminium (Fe-15Cr-5Al)

The mass gains of Fe-15Cr-5Al in the exposure tests are very similar to those of Fe-15Cr-5Si (Fig. 2). In this case a nearly protective Al_2O_3 -layer forms and only local attack by active oxidation is observed, for 500 vppm HCl as well as for 1500 vppm HCl. Fig. 15a shows a cross sectional micrograph of the corroded specimen with the complete oxide scale. From XRD analysis, γ - Al_2O_3 and Fe_2O_3 are the phases detected in the oxide layer. In the cross section the dark regions near the surface were identified as Al_2O_3 .

This positive corrosion behaviour is not reliable for experiments at higher gas velocities. Fig. 15b shows a cross section of a corroded specimen after a thermogravimetric experiment. High mass gains occur by strong active oxidation, resulting in a multilayered corrosion scale of Al_2O_3 , Cr_2O_3 and Fe_2O_3 . Fig. 16 compares the results for a ground and a polished surface. It is visible that higher mass gains due to active oxidation are observed for the ground sample. Concerning the influence of the surface treatment on the formation of chlorides no studies have yet been performed. Within this work, it was observed for the ferritic alloys, that a favoured nucleation of chlorides occurs at physical defects, such as grinding patterns, scratches, sample edges or edges of grain boundaries.

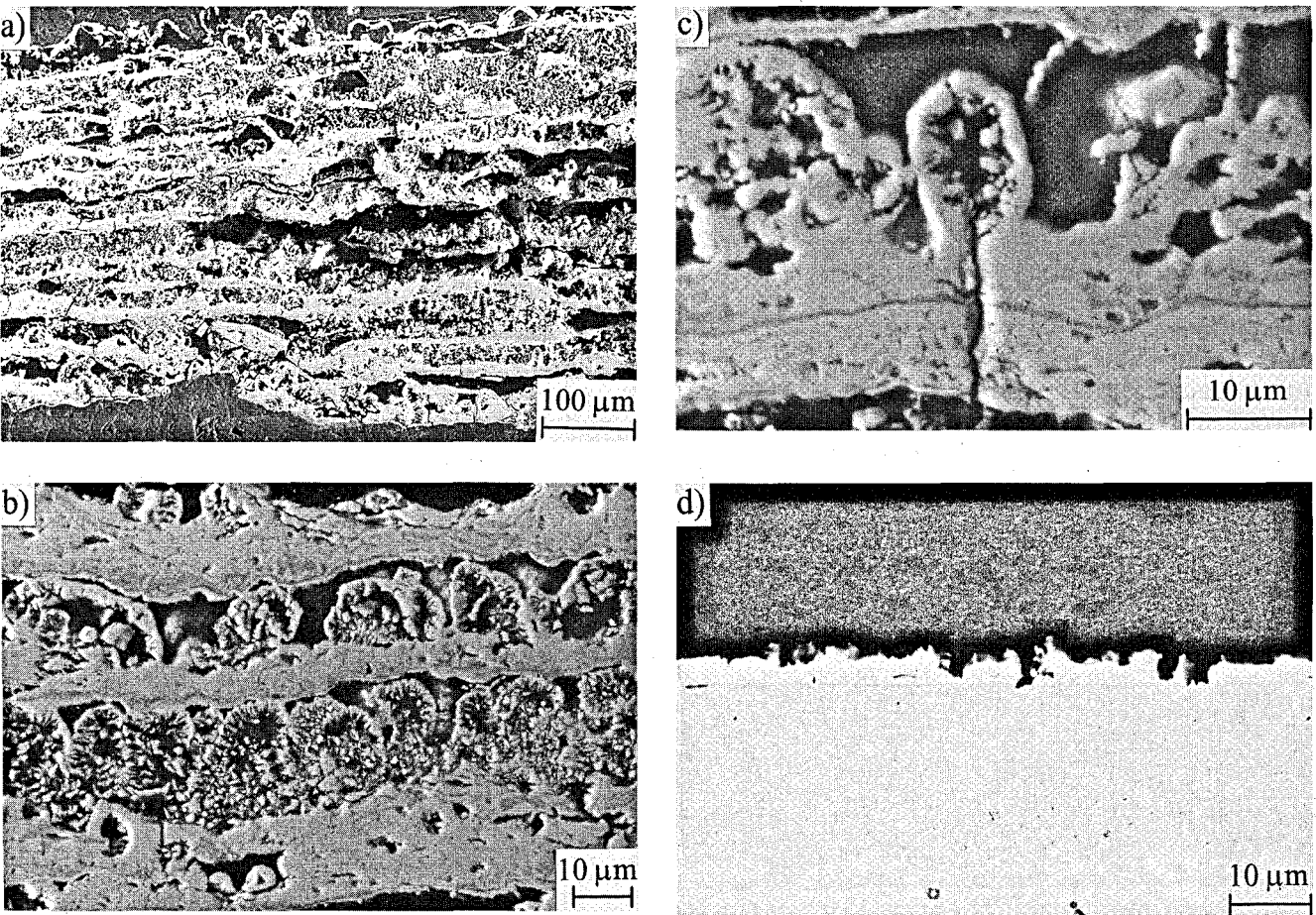


Fig. 11. SEM micrographs of corroded Fe-15Cr-5Ti specimens after 168 h exposure in N₂-5 % O₂-(500/1500) vppm HCl. a) Cross section of the entire corrosion layer (1500 vppm HCl). b) Details of the corrosion scale showing the features of the schematic mechanism presented in Fig. 5 (500 vppm HCl). c) Fe-rich oxide formed over a crack in a compact oxide layer by "active oxidation" (500 vppm HCl). d) Cross section of the specimen after removal of the corrosion layer. Precipitates of a titanium enriched intermetallic phase (light regions) are visible

Abb. 11. REM Aufnahmen von korrodierten Fe-15Cr-5Ti Proben nach 168 h Auslagerung in N₂-5 % O₂-(500/1500) vppm HCl. a) Querschliff der gesamten Korrosionsschicht (1500 vppm HCl). b) Ausschnitt der Korrosionsschicht, mit den charakteristischen Morphologien des in Fig. 5 dargestellten schematischen Modells (500 vppm HCl). c) Fe-reiches Oxid, das sich durch „aktive Oxidation“ über einem Spalt einer kompakten Oxidschicht gebildet hat (500 vppm HCl). d) Querschliff von der Probe nach Abtrag der Korrosionsschicht. Ausscheidungen einer Titan-angereicherten intermetallischen Phase (helle Bereiche) sind sichtbar

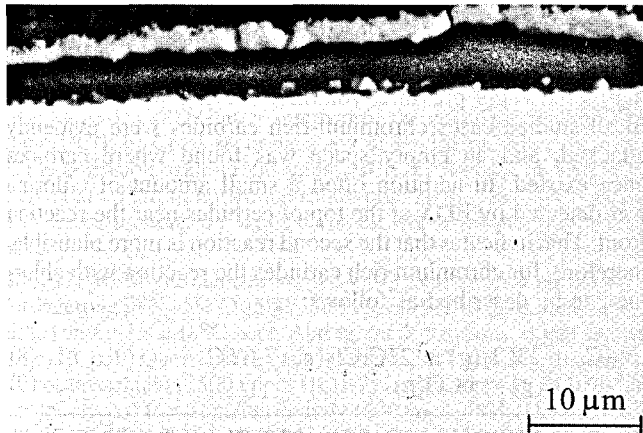


Fig. 12. SEM micrograph of a cross-section of Fe-15Cr-5Si after 168 h of exposure in N₂-5 % O₂-1500 vppm HCl
Abb. 12. REM Aufnahme eines Querschliffes von Fe-15Cr-5Si nach 168 h Auslagerung in N₂-5 % O₂-1500 vppm HCl

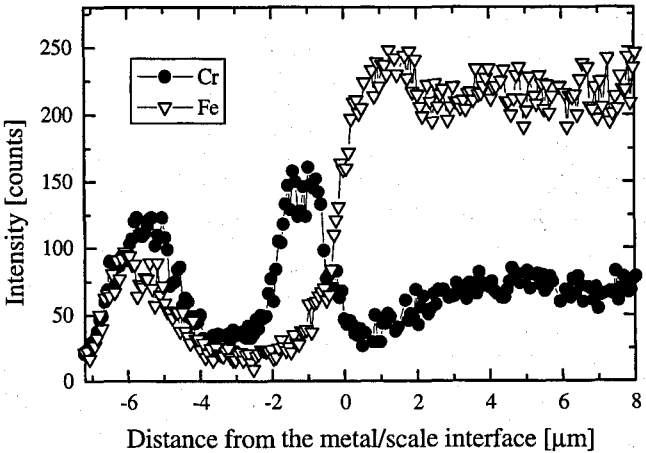


Fig. 13. EDX linescan through the corrosion scale and metal of Fe-15Cr-5Si after exposure in N₂-5 % O₂-1500 vppm HCl
Abb. 13. EDX-Linescan durch die Korrosionsschicht und die Metalloberfläche von Fe-15Cr-5Si nach 168 h Auslagerung in N₂-5 % O₂-1500 vppm HCl

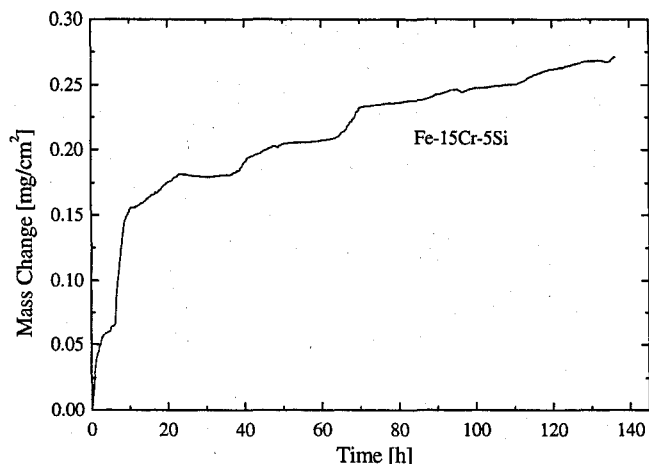


Fig. 14. Results of the thermogravimetric experiments for Fe-15Cr-5Si in He-5 % O₂-500 vppm HCl

Abb. 14. Ergebnisse der thermogravimetrischen Experimente für Fe-15Cr-5Si in He-5 % O₂-500 vppm HCl

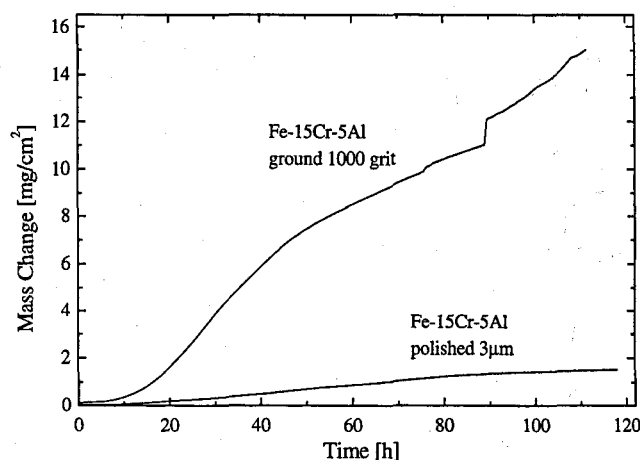


Fig. 16. Thermogravimetric results for Fe-15Cr-5Al in He-5 % O₂-500 vppm HCl after different surface treatments

Abb. 16. Thermogravimetrische Ergebnisse für Fe-15Cr-5Al in He-5 % O₂-500 vppm HCl nach unterschiedlichen Oberflächenbehandlungen

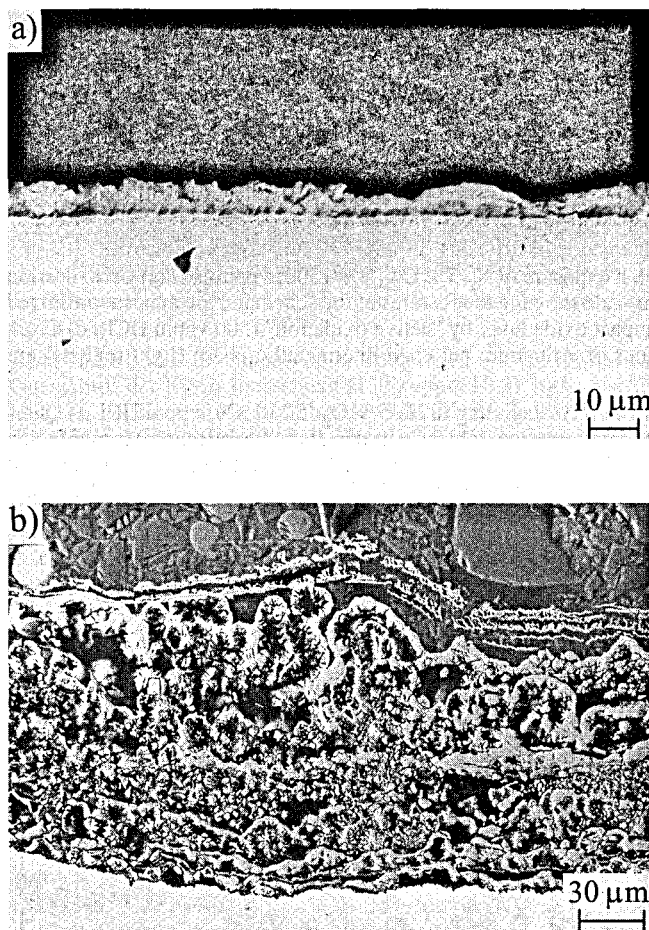


Fig. 15. a) SEM micrograph of a cross-section of Fe-15Cr-5Al after 168 h of exposure in N₂-5 % O₂-1500 vppm HCl. b) SEM micrograph of a cross-section of Fe-15Cr-5Al (ground surface) after 137 h of exposure in He-5 % O₂-500 vppm HCl

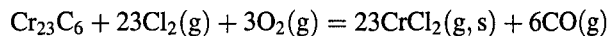
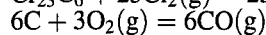
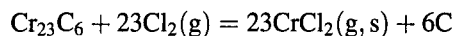
Abb. 15. a) REM Aufnahme eines Querschliffes von Fe-15Cr-5Al nach 168 h Auslagerung in N₂-5 % O₂-1500 vppm HCl. b) REM Aufnahme eines Querschliffes von Fe-15Cr-5Al (geschliffene Oberfläche) nach 137 h Versuchsdauer in He-5 % O₂-500 vppm HCl

From these results the ground surface promotes the formation of chlorides and, therefore, prevents the formation of a protective Al₂O₃-layer, resulting in the observed behaviour.

3.4.7 The effect of carbon

Regardless of the chromium content in the matrix and the carbide morphology, chromium rich carbides were attacked preferentially in comparison to the matrix (Figure 17a–c). In the Fe-15Cr-0.8C alloy (Fig. 17a), the M₂₃C₆ carbides appear as dark regions within matrix, which obviously are consumed by corrosion. In the case of Fe-35Cr-C, the M₂₃C₆ carbides (darker gray) surround an inner metallic core (Fig. 17b) which is more stable whereas the carbides are preferentially attacked. From a surface SEM micrograph (Fig. 17c), holes and channels can be seen where previously carbides were situated indicating volatilization of metal chlorides.

Two possibilities exist for the reaction of the carbides with the O₂/HCl atmosphere: (1) the carbides react with oxygen to form oxides or (2) the carbides react with chlorine to form chlorides. In the first case, solid oxides would form on the carbides and they should be detectable. In the second case, solid chlorides form, which either remain as solids or, depending on the vapor pressure, volatilize leaving an empty space. In all studied cases chromium-rich carbides were evidently attacked, and an empty space was found where carbides once existed. In addition often a small amount of chlorine was detected by EDX at the top of carbides near the reaction front. This indicates that the second reaction is more plausible therefore, for chromium rich carbides the reaction with chlorine can be described as follows:



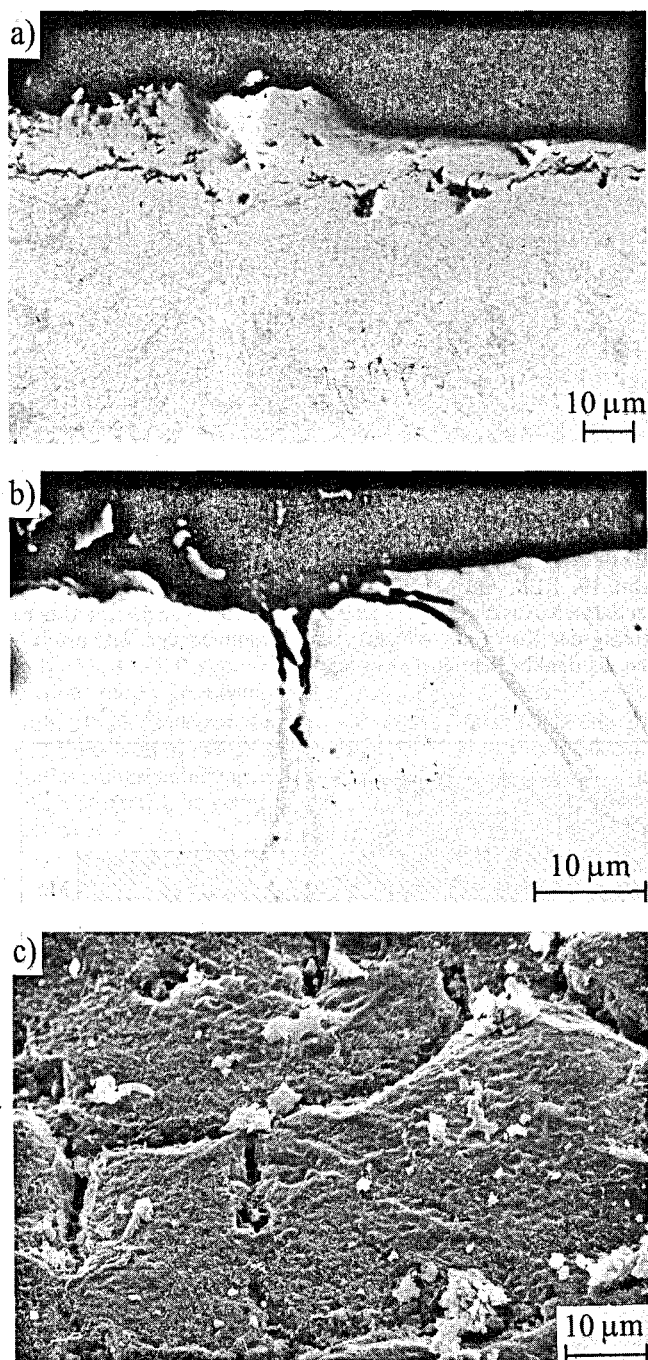


Fig. 17. SEM micrographs of Fe-Cr-C alloys exposed at 600 °C in N_2 -5 % O_2 -(500/1500) vppm HCl for 168 hours. a) Cross-sectional view of Fe-15Cr-0.8C after removal of the corrosion scale (1500 vppm HCl), b) Cross-sectional view of Fe-35Cr-C after removal of the corrosion scale (1500 vppm HCl). c) Surface of Fe-35Cr-C tilted at 45° from horizontal (500 vppm HCl). The dark regions in the cross-sections are $M_{23}C_6$ carbides, which are attacked preferentially

Abb. 17. REM Aufnahmen von Fe-Cr-C Legierungen nach 168 h Auslagerung in N_2 -5 % O_2 -500/1500 vppm HCl. a) Querschliff-Ansicht von Fe-15Cr-0,8C nach Abtrag der Korrosionsschicht (1500 vppm HCl). b) Querschliff-Ansicht von Fe-35Cr-C nach Abtrag der Korrosionsschicht (1500 vppm HCl). c) Oberfläche von Fe-35Cr-C um 45° aus der Horizontalen gedreht (500 vppm HCl). Die dunklen Bereiche in den Querschliffen sind $M_{23}C_6$ -Carbide, die bevorzugt angegriffen werden

The carbide reacts with chlorine to form chromium chloride and carbon (Eqn. 8). The carbon can subsequently react with oxygen at the low oxygen pressure to form CO gas (Eqn. 9). The overall reaction can thus be described by Eqn. 10. Due to the high equilibrium vapor pressure, the solid chloride volatilizes (Eqn. 11).



For simplicity, only $CrCl_2$ is considered, but other chlorides (e.g. $CrCl_3$ and $FeCl_2$) may form. The high reactivity of the $M_{23}C_6$ carbides is probably caused by the high chromium contents not leading to a formation of protective chromium oxide.

Though clearly preferential attack of the chromium rich carbides was observed, no correlation between high carbide contents and higher corrosion rate was found. In fact, it can be seen from Fig. 2 that, especially for 500 vppm HCl, smaller mass gains were observed in Fe-Cr alloys with carbon relative to those without, due to better adherence of the formed oxide layer.

The corrosion behaviour of the molybdenum rich M_6C carbides in Fe-15Cr-10Mo-C is very different from the behaviour of the chromium rich carbides. These carbides are more stable than the matrix and the regions surrounding the carbides are attacked preferentially. Figure 18a shows a cross section of a corroded specimen after removal of the corrosion products in which the carbides appear as the light regions. On the surface the stable carbides are visible within the very porous molybdenum enriched metal scale (Fig. 18b). The stability of the carbides is caused by the high molybdenum contents. This is consistent with the matrix corrosion, where chromium and iron are very reactive while molybdenum is more resistant.

Figure 19 shows the micrograph of a corroded specimen of Fe-15Cr-5Ti-C with precipitations of dark precipitates of TiC. In this case no clear distinction between the corrosion behaviour of the matrix and the carbides was observed. Neither a susceptible behaviour as for the chromium rich $M_{23}C_6$ carbides nor a resistant behaviour as for the molybdenum rich M_6C occurs at 600 °C. In the near-surface regions the carbides are partly surrounded by empty space. It is not yet clear if the carbides are preferably attacked themselves or if the surrounding metal is attacked.

3.5 Behaviour of the different elements in the active oxidation process

According to the thermodynamic considerations in section 3.1, it is expected that the alloying elements behave very different concerning the active oxidation process. Volatilizing chlorides which do not convert into oxides within the scale are transported with the gas flow and condense as solid products in cooler regions of the furnace tube. The metal composition of this deposit was analyzed after an experiment with 1500 vppm HCl and the ratios of metal percentages in the deposit and metal percentages of all specimens included in the experiment, one sample of each alloy in Table 1, are shown in Figure 20. The amount of aluminium, silicon and titanium detected in the deposits was too small for an analysis with ICP-OES (Inductively Coupled Plasma-Optical Emission Spectroscopy). The amount and also the composition of the metal chloride sublimating to the outlet of the furnace strongly depends on the stability of the considered chloride on the metal substrate, its vapour pressure and especially its sta-

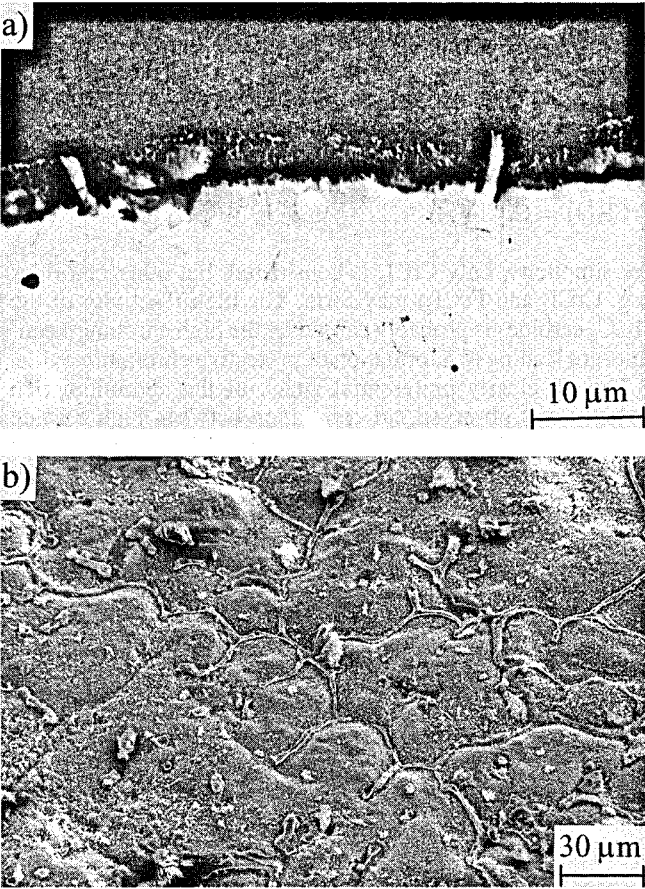


Fig. 18. SEM micrographs of Fe-15Cr-10Mo-C exposed at 600 °C in N₂-5 % O₂-1500 vppm HCl for 168 h after removal of the corrosion scale. a) Cross-sectional view. b) Surface tilted at 45° from horizontal. The Mo-rich M₆C carbides (light regions) are stable relative to the surrounding metal

Abb. 18. REM Aufnahmen von Fe-15Cr-10Mo-C ausgelagert bei 600 °C in N₂-5 % O₂-1500 vppm HCl für 168 h C nach Abtrag der Korrosionsschicht. a) Querschliff-Ansicht. b) Oberfläche um 45° aus der Horizontalen gedreht. Die Mo-reichen M₆C-Carbide (helle Bereiche) sind stabil relativ zum umgebenden Metall

bility with respect to the conversion into oxide during evaporation. From the results in Fig. 20 it is visible that prevalingly manganese chlorides volatilize from the specimen and iron chlorides more than chromium chlorides. These experimental results are in good correspondence to the great differences of the thermodynamic values listed in Table 3 concerning the conversion of the evaporating chlorides into oxides. The relevant oxygen pressures for the conversion of CrCl₂ ($2.41 \cdot 10^{-18}$ bar) and MnCl₂ ($7.59 \cdot 10^{-5}$ bar) differ by a factor of about $3 \cdot 10^{13}$, which means that CrCl₂ is converted into oxide much easier than MnCl₂. In comparison to these great differences, the differences concerning the formation and the vapour pressures of the chlorides have much smaller influence on the observed values in Fig. 20.

The high molybdenum content in the deposits is caused most probably by the evaporation of MoO₃, as molybdenum chlorides are converted into oxides at low oxygen pressures and the vapour pressure of MoO₃ is relatively high. For titanium, aluminium and silicon it is difficult to make any conclusions, because on the one hand the amounts of these species

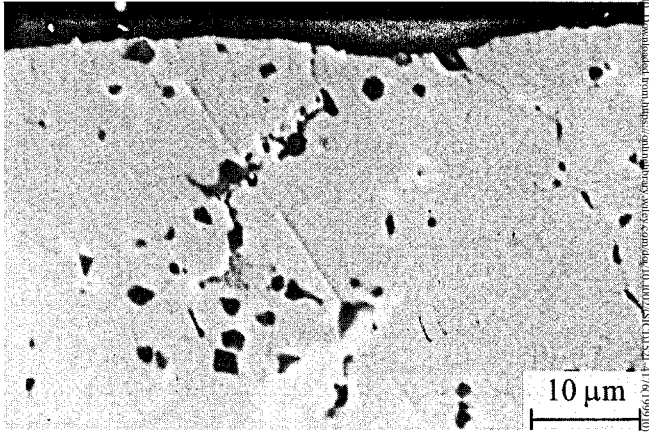


Fig. 19. SEM micrograph of a cross-section of Fe-15Cr-5Ti-C after 168 h of exposure in N₂-5 % O₂-1500 vppm HCl and after removal of the corrosion scale. Precipitations of TiC carbides appear as dark areas

Abb. 19. REM Aufnahme eines Querschliffes von Fe-15Cr-5Ti-C nach 168 h Auslagerung in N₂-5 % O₂-1500 vppm HCl und nach Abtrag der Korrosionsschicht. Ausscheidungen von TiC erscheinen als dunkle Bereiche

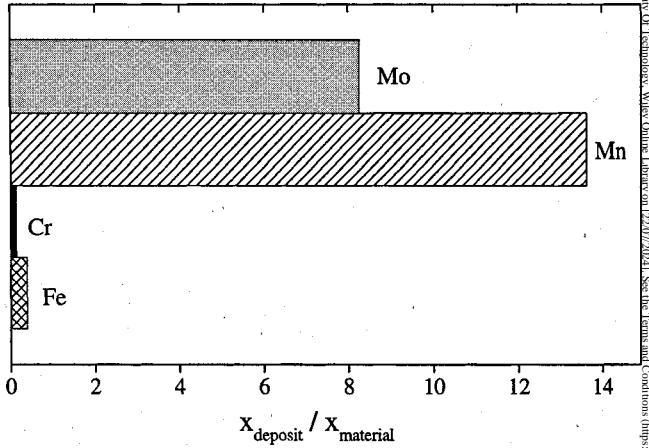


Fig. 20. Results of the chemical analysis of deposits found in the furnace tube after an exposure experiment in 1500 vppm HCl, presented as a ratio of amount of element in the deposit, x_{deposit} , relative to the total amount of the element in the alloys, x_{material}

Abb. 20. Ergebnisse der chemischen Analyse des Ofenrohrbelages nach einem Auslagerungsexperiment bei 1500 vppm HCl. Dargestellt ist das Verhältnis der Elementgehalte im Belag, x_{deposit} , normiert auf die Gesamtmenge des Elements in den Legierungen x_{material}

in the material were very small, and on the other hand their chlorides remain in the gaseous state down to very low temperatures, so that it is not sure if they condense completely at the furnace tube. From the thermodynamic considerations, very small amounts of evaporating chlorides would be expected, since the necessary oxygen partial pressures for the conversion of the chlorides are very low (Tab. 3).

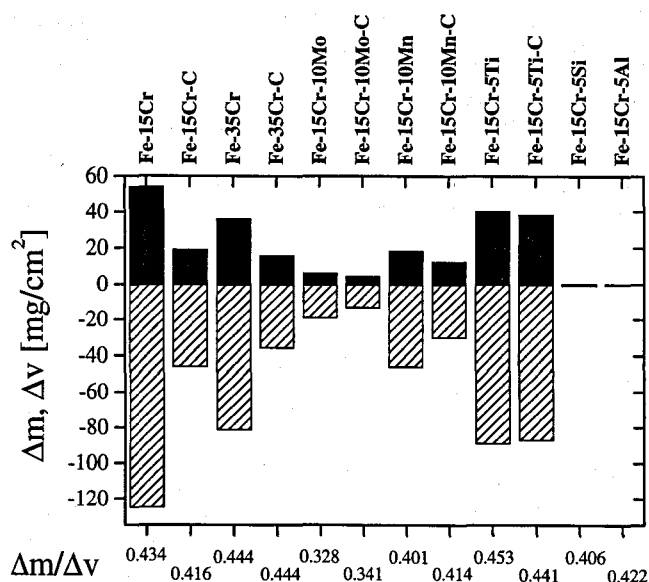


Fig. 21. Comparison between total mass change Δm and metal loss Δv after removal of the corrosion products for an exposure at 600 °C in N_2 -5 % O_2 -500 vppm HCl. Additionally the values for the proportion $\Delta m/\Delta v$ are given

Abb. 21. Gegenüberstellung von absoluter Massenänderung Δm und Metallverlust Δv nach Entfernen der Korrosionsprodukte für Auslagerungsbedingungen bei 600 °C in N_2 -5 % O_2 -500 vppm HCl. Zusätzlich angegeben sind die Werte für das Verhältnis $\Delta m/\Delta v$

3.6 Quantitative analysis of the amount of evaporating corrosion products

In order to quantify the extent of corrosion, the metal loss after complete removal of the corrosion products can be used. For small corrosion rates and especially for well adherent corrosion layers, exact values are difficult to determine. In these cases it is easier and more exact to measure the total mass gain, as it was done within this study. If corrosion products evaporate from the sample, the measured mass increase does not correspond to the total amount of formed corrosion products, and therefore would have no quantitative value for the corrosion extent. The values in Figure 20 give only information about which corrosion products volatilize preferentially but these values are not quantified. To determine the relative amount of metal loss due to volatilizing metal chlorides additional metal loss measurements were made. In Fig. 21 total mass changes are presented in comparison to the observed mass losses for an experiment in N_2 -5 % O_2 -500 vppm HCl. The x-axis provides the values of the ratio of mass change to mass loss, $\Delta m/\Delta v$. By comparing the observed results with the theoretically expected values for complete conversion of chlorides into oxides, the amount of volatilizing corrosion products can be determined. Theoretically for Fe_2O_3 0.429, for Cr_2O_3 0.461 and for Mn_2O_3 0.437 are the expected ratios $\Delta m/\Delta v$ concerning the oxide formation from the metals. The ratios for the formation of spinels are lower and for TiO_2 , Al_2O_3 and SiO_2 higher (> 0.6). Totally evaporating corrosion products correspond to a $\Delta m/\Delta v$ -value of 1 and, therefore, evaporating corrosion products lead to a decreasing ratio. For Fe-15Cr, Fe-35Cr and Fe-15Cr-5Ti the experimental ratios show that there is no significant loss of volatile products, as the values are very near to those expected

for complete conversion to the found oxides. In the cases of Fe-15Cr-10Mo, Fe-15Cr-10Mn, Fe-15Cr-5Si and Fe-15Cr-5Al the ratios are smaller than for the complete conversion, but the reasons are very different. For Fe-15Cr-10Mn the ratio is decreased due to a significant evaporation of $MnCl_2$, which corresponds to the results from section 3.5. The small observed ratio for Fe-15Cr-10Mo has two reasons. On the one hand the value is decreased due to evaporating molybdenum oxide and on the other hand during the removal of the corrosion products probably parts of the very porous molybdenum enriched metal zone were also removed, which leads to a smaller ratio. Considering Fe-15Cr-5Si and Fe-15Cr-5Al thin corrosion scales are formed and it is much easier for evaporating chlorides to leave the sample than in the case of thick corrosion scales, which leads to a higher portion of evaporating products. In general, it was observed that for iron and chromium the amount of evaporating chlorides is very small and the conversion into oxides is nearly complete. Observations for a higher HCl content of 1500 vppm were not significantly different and confirmed the results obtained for 500 vppm HCl.

4 Summary

Some important features of the corrosion of ferritic iron chromium alloys occurring in chlorine containing oxidizing atmospheres at 600 °C have been presented. The influences of additional alloying elements on the corrosion behaviour were investigated and discussed. In the case of chromium, the influence is strongly dependent on the alloy composition leading either to porous, multilayered scales or to the formation of a protective layer as for Fe-15Cr-5Si. The highest extent of corrosion was observed for the binary iron-chromium alloys, where the corrosion mechanism is characterized by a frequent spalling of the scale and alternating dense and porous oxide layers are found within the scale. Silicon was found to promote the formation of more protective Cr_2O_3 layers and, therefore, has a very positive influence on the corrosion resistance. Molybdenum as an alloying element causes a more resistant behaviour and decreases the total corrosion rate. In Fe-15Cr-10Mo preferential oxidation of the more reactive elements chromium and iron was observed. Additions of aluminium may lead to the formation of protective Al_2O_3 , but this is strongly dependent on the experimental conditions. Manganese and titanium show a very reactive behaviour concerning the active oxidation process. Thermodynamic considerations for the behaviour of the different elements in the active oxidation process have been presented and compared with the experimental results.

Chromium rich carbides were found to be preferentially attacked relative to the matrix, whereas molybdenum rich carbides were more resistant than the surrounding matrix.

5 Acknowledgments

The authors would like to thank A. Schneider for thermodynamic calculations with Thermo-Calc, H. Viehhaus for AES and XPS measurements, E. Zentara for SEM analysis and K. Hennessen and W. Vogt for performing XRD measurements. The support of the Deutsche Forschungsgemeinschaft is gratefully acknowledged.

6 References

- [1] M. Spiegel, H. J. Grabke: *Materials and Corrosion* 46 (1995) 121.
- [2] M. Spiegel, H. J. Grabke: *Materials and Corrosion* 47 (1996) 179.
- [3] Y. Ihara, H. Ohgame, K. Sakiyama, K. Hashimoto: *Corr. Sci.* 21 (1981) 805.
- [4] N. S. Jacobsen: *Oxidation of Metals* 26 (1986) 157.
- [5] F. H. Stott, R. Prescott, P. Elliott: *Werkst. Korros.* 39 (1988) 401.
- [6] Y. Y. Lee, M. J. McNallan: *J. Electrochem. Soc.* 137 (1990) 472.
- [7] K. N. Strafford, P. K. Datta, D. Forster: *Corr. Sci.* 29 (1989) 703.
- [8] Y. Ihara, H. Ohgame, K. Sakiyama, K. Hashimoto: *Corr. Sci.* 23 (1983) 167.
- [9] K. Reinhold, K. Hauße: *J. Electrochem. Soc.* 124 (1977) 875.
- [10] Y. Shinata, M. Hara, T. Nakagawa: *Mat. Trans., JIM* 32 (1991) 969.
- [11] Y. Ihara, H. Ohgame, K. Hashimoto: *Corr. Sci.* 25 (1984) 96.
- [12] D. Bramhoff, H. J. Grabke, H. P. Schmidt: *Werkst. Korros.* 40 (1989) 642.
- [13] X. Zheng, R. A. Rapp: *Oxidation of Metals* 48 (1997) 527.
- [14] A. S. Kim, M. J. McNallan: *Corrosion* 46 (1990) 747.
- [15] M. J. McNallan, A. S. Kim, J. C. Liu, S. Thongtem, S. Y. Lee: *High Temperature Corrosion in: Corrosion Science and Engineering*, R. A. Rapp, N. A. Golecen, A. Pourbaix, eds., Vol. 1, Cebelcor, Brüssel, (1989) p. 113.
- [16] Y. Sato, M. Hara, Y. Shinata, T. Narita: *Journal of the Japan Institute of Metals* 60 (9) (1996) 841.
- [17] D. Bramhoff, H. J. Grabke, E. Reese, H. P. Schmidt: *Werkst. Korros.* 41 (1990) 303.
- [18] M. Spiegel, H. J. Grabke: *Materials and Corrosion* 46 (1995) 121.
- [19] H. J. Grabke, E. Reese, M. Spiegel: *Corr. Sci.* 37 (1995) 1023.
- [20] D. A. Berziss, M. Spiegel, H. Viehhaus, A. Schneider, H. J. Grabke: in: *Proceedings of the European Federation of Corrosion, Event No. 208, EUROCORR '97* (1997) Vol II., 29.
- [21] H. Fujikawa, N. Maruyama: *Mat. Sci. and Eng. A120* (1989) 301.
- [22] P. Gawenda; A. Rahmel, K. Raths, M. Schorr, U. Schultz, A. Weiser: *Materials and Corrosion* 48 (1997) 176.
- [23] M. J. McNallan, S. Thongtem, J. C. Liu, Y. S. Park, P. Shyu: *J. de Physique IV* 3 (1993) 143.
- [24] J. M. Abels, H. H. Strehblow: *Corr. Sci.* 39 (1997) 115.
- [25] A. Roine: *HSC Chemistry Ver. 203*, Outokumpu Research Oy Pori, Finland, (1994).
- [26] O. Knacke, O. Kubaschewski, K. Hesselmann: *Thermochemical Properties of Inorganic Substances*, Düsseldorf: Verlag Stahleisen mbH, (1991).
- [27] M. J. McNallan, W. W. Liang, S. H. Kim, C. T. Kang: in: *High Temperature Corrosion*, ed., R. A. Rapp NACE 1983, p. 316.
- [28] Y. Y. Lee, M. J. McNallan: *Metallurg. Trans. 18A* (1987) 1099.
- [29] B. Sundman, B. Jansson, J.-O. Andersson: *CALPHAD* 9 (1985) 153.
- [30] P. Villars, A. Prince, H. Okamoto: *Handbook of Ternary Phase Diagrams*, Vol. 7, ASM International, 1995.
- [31] R. N. Durham, B. Gleeson, D. J. Young: *Oxidation of Metals* 50 (1998) 139.
- [32] G. C. Wood, J. A. Richardson, M. G. Hobby: *J. Boustead, Corr. Sci.* 9 (1969) 659.
- [33] G. R. Johnston: *High Temp. – High Press.* 14 (1982) 695.
- [34] A. A. Soloshenko, Y. E. Vil'nyanskii: *Russ. J. Inorg. Chem.* 14 (7) (1969) 1045.
- [35] E. Reese: *Dissertation Universität Dortmund*, 1992.
- [36] H. W. Pickering: *Corrosion Problems in Energy Conversion and Generation*, The Electrochemical Soc. (1974) p. 151.
- [37] C. D. Wagner, W. M. Riggs, L. E. Davis, J. F. Moulder, G. E. Muilenberg (Eds.): *Handbook of X-Ray Photoelectron Spectroscopy*, Eden Prairie, 1978.

(Received: March 11, 1999)

W 3359

Amelinckx, S./Van Dyck, D./Van Landuyt, J./ Van Tendeloo, G.

Handbook of Microscopy

Applications in Materials Science, Solid-State Physics, and Chemistry

Volume Methods I

1997. XXIV, 573 pages with 374 figures, 4 in color and 8 tables. Hardcover. ISBN 3-527-29280-2

Volume Methods II

1997. XXV, 482 pages with 255 figures, 7 in color and 19 tables. Hardcover. ISBN 3-527-29473-2

Volume Applications

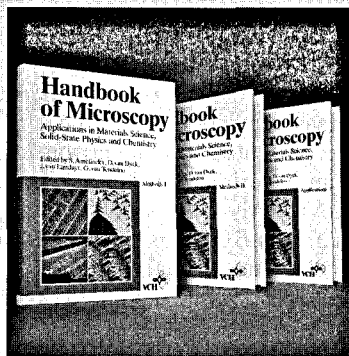
1997. XXXI, 877 pages with 666 figures, 12 in color and 54 tables. Hardcover. ISBN 3-527-29293-4

Price per volume: DM 525.00/US\$ 383.00/SFr 467.00

Set price: DM 1275.00/US\$ 930.00/1134.00

ISBN 3-527-29444-9

WILEY-VCH, P.O. Box 10 11 61, 69451 Weinheim, Germany.
Fax: +49 (0) 62 01-60 61 84, e-mail: sales-books@wiley-vch.de



The new
global
force in
scientific
publishing



WILEY-VCH